ACS Catalysis

Research Article

pubs.acs.org/acscatalysis

On the Mechanism of the Catalytic Binuclear Elimination Reaction in Hydroformylation Systems

Marco Klähn* and Marc V. Garland*

Institute of Chemical and Engineering Sciences, Agency for Science, Technology and Research, 1 Pesek Road, Jurong Island, 627833, Republic of Singapore

Supporting Information

ABSTRACT: A number of phenomenological reasons exist for synergism in mixed metal-mediated homogeneous catalysis. In the catalytic binuclear elimination reaction (CBER), the unusual high-activity system possesses mononuclear intermediates of each metal as well as dinuclear intermediates. All of these intermediates act in a synchronized and concerted manner to transform substrates to products. Detailed in situ spectroscopic measurements (Li, C.; Widjaja, E.; Garland, M. *J. Am. Chem. Soc.* **2003**, *125*, 5540−5548. Li, C.; Chen, L.; Garland, M. *J. Am. Chem. Soc.* **2007**, *129*, 13327−13334. Li, C.; Cheng, S.; Tjahjono, M.; Schreyer, M.; Garland, M. *J. Am. Chem. Soc.* **2010**, *132*, 4589−4599) have repeatedly confirmed that for rhodium−rhenium and rhodium−manganese hydroformylation systems, the product rate, r, can be described with $r = [Rh(CO)_4RCO]^1(k_\alpha[CO]^{-1.0}[H_2]^1 + k_\beta[CO]^{-1.6}[HM(CO)_5]^1)$. The apparent rate constants, k_α and k_β, highlight a distinction between contributions from the classic unicyclic rhodium-mediated hydroformylation reaction and the rhodium−rhenium/manganese CBER. Molecular simulations are carried out to find the underlying mechanisms causing this inexplicable rate expression. Free energy surfaces describing rhodium−rhenium-catalyzed hydroformylation are derived with DFT, on which reaction paths are identified and characterized. In molecular dynamics simulations, nonchemical rhodium−rhenium association is observed, and its strength is determined. The CBER proceeds via three reaction steps: (1) dissociation of one carbonyl from the rhodium complex to enable binding of rhenium, (2) transfer of hydrogen from rhenium to rhodium, and (3) transfer of hydrogen from rhodium to the hydroformylation substrate. The CBER is enabled by a stabilization of bimetallic intermediates by ∼7 kcal/mol, compared with unicyclic hydroformylation with H_2. This is accomplished by coordinatively saturating rhodium with electron-rich rhenium. Moreover, a solvophobic effect in nonpolar solvents facilitates nonchemical rhodium−rhenium association. This increases locally the rhenium concentration in the vicinity of rhodium and thereby acts as a secondary catalytic effect. Overall, three interconnected catalytic cycles are identified: one cycle involves the classic mononuclear intermediates, whereas the two other cycles describe two distinct CBER pathways, in which rhenium−rhodium binding occurs either before or after acylation of the hydroformylation substrate. A combination of these three catalytic cycles reproduces all salient features of experimental observations successfully, thereby confirming the newfound intermediates, reaction mechanisms, and factors that cause the catalytic effect of CBER.

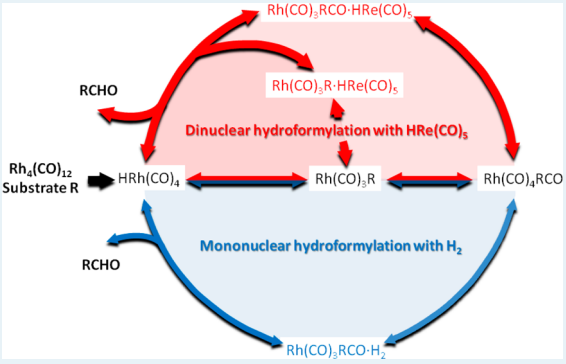

KEYWORDS: *Hydroformylation, CBER, binuclear elimination, metal organic catalysis, homogenous catalysis, molecular simulation, DFT, MD, molecular dynamics, free energy surface, bimetallic catalysis*

1. INTRODUCTION

Homogeneous catalytic metal-mediated organic synthesis has developed into an area of enormous importance for synthetic chemistry. This importance lies in the high degree of chemo-, regio-, and stereoselective control that can be exerted by the use of well-defined organometallics as catalyst precursors.[1−5] The main focus of most homogeneous catalytic work has been directed toward its synthetic applications, and it is has been common practice to test various organometallic precursors and ligand precursor combinations to achieve the target synthetic reaction with desired selectivity and activity. To survey possible usefulness, mononuclear or homometallic polynuclear precursors have been the default starting point and even scope of most studies. Extensions to bimetallic or multimetallic precursors (or combinations of different homometallic complexes) have, on occasion, resulted in quite unusual synthetic observations. The combined application of more than one metallic element in homogeneous catalysis and synthetic results which differ greatly from a strictly additive effect is commonly referred to under the collective term "synergism". Because detailed mechanistic studies and, hence, understanding of the latter systems are rather rare, and because

Received: August 30, 2014
Revised: February 20, 2015
Published: March 12, 2015

© 2015 American Chemical Society

DOI: 10.1021/cs5019925
ACS Catal. 2015, 5, 2301−2316

quite unusual synthetic results have on occasion been observed, bimetallic and multimetallic systems appear to provide considerable research opportunities for identifying new, previously unknown and unexpected phenomenological origins for reactivity patterns.

The simplest reaction topology for a general homogeneous catalytic system involves a unicyclic connectivity of the intermediates, and some of these intermediates on the cycle may be in rapid equilibrium exchange with organometallic species immediately adjacent.[1] This simplest topology has two interrelated consequences: namely, each soluble intermediate (including species in rapid equilibrium exchange) has one-and-the-same nuclearity (i.e., all mononuclear, or all dinuclear etc.), and intermediates do not react together to produce other intermediates. The mathematical description of the activity of such as system, in the approximation of a steady state or pseudosteady state product formation rate, r = $\dot{P}$, can be expressed in terms of either the concentration of each and every jth intermediate, I_j (eq 1), or with the total sum of all intermediate concentrations (eq 2), where the terms k_j^* and k_{TOF} contain only constants and terms involving reactant concentrations (but not concentrations of organometallics):

$$r = k_j^*[I_j] \ \forall \ j \tag{1}$$

$$r = k_{TOF} \sum_j [I_j] \tag{2}$$

Specifically, the latter expression, eq 2, is useful as the formal definition for the well-known turnover frequency (TOF) of a reaction cycle, especially when it is evaluated in terms of instantaneous reaction rates and intermediate concentrations at any time, t. This result was originally derived by King and Altman using matrix algebra in the context of enzyme kinetics[6] and has been expanded by others.[7−9] The most central and important concept concerning unicyclic mechanisms is that the resulting system activity is *linear* in intermediate concentrations.

Organometallic intermediates have been observed for unicyclic homogeneous metal-mediated organic syntheses using in situ spectroscopic methods. Quite notable contributions to this area have been made: (1) identification of a key intermediate $MeRh(CO)_2I_3$ for the rhodium-catalyzed carbonylation of methanol to acetic acid using FTIR;[10] (2) study of various phosphite-modified rhodium hydroformylation systems with FTIR and NMR;[11] (3) elucidation of the mechanisms of Pd-catalyzed synthesis of methyl propionate from ethylene and carbon monoxide (Lucite Alpha process), the Pd-catalyzed oligomerization from ethylene and carbon monoxide (Shell process for polyketones), and the Rh catalyzed hydrogenation of methacycline to give doxycycline (Hovione process),[12−14] all using in situ NMR; (4) study of various modified rhodium catalyzed hydroformylation reactions using FTIR;[15] and (5) the use of parahydrogen and NMR for a variety of systems.[16,17] More recently, criteria have been identified and implemented to confirm, beyond any reasonable doubt, that an observable organometallic is, in fact, an intermediate. A crucial part of this procedure is the evaluation of eq 1 using in situ spectroscopic data.[18] Indeed, the validity of eqs 1 and 2 in homogeneous metal-mediated syntheses has been experimentally confirmed by in situ spectroscopic studies.[19,20]

In contrast, only a very few well-described and reproducible *nonlinear* correlations of rates in terms of metal/intermediates, have been noted from kinetic studies of homogeneous catalytic metal-mediated organic syntheses.[21−25] These nonlinear correlations appear to fall into four broad categories, in which the product rate is (i) quadratic in total metal/intermediate concentrations;[26,27] (ii) linear−quadratic in metal/intermediate concentrations;[28−32] (iii) bilinear in metal/intermediate concentrations, that is, carbonylation;[33] and (iv) linear−bilinear in metal/intermediate concentrations, that is, hydroformylation.[34−40] Such nonlinear rate dependencies do not appear to arise in systems where there is cooperativity between neighboring metal centers existing on the same large multidentate ligand (because the metal ratios are constant), although quite unusual selectivity patterns have been observed.[41,42] The first two categories, i and ii, belong to homometallic systems, whereas categories iii and iv strictly belong to heterobimetallic systems.

Although detailed in situ spectroscopic investigations of homogeneous catalytic systems are still not very common,[43] both the linear−bilinear carbonylation of methanol to acetic acid using Ir−Ru (the Cativa process)[33] and the linear−bilinear Rh−Mn, Rh−Re, Rh−Mo, and Rh−W hydroformylations of alkenes have been studied extensively with in situ infrared spectroscopy.[34−40] In the Cativa process, it has been clearly shown that ruthenium serves to abstract chlorine from an iridium complex, thereby opening a new coordination site. In contrast, the hydroformylation studies indicate direct attack of a metal hydride HML_n leading to product formation, where H is incorporated into the final product. In particular, the hydroformylation studies clearly demonstrated the general functional form in eq 3, where $Rh(CO)_4RCO$ was the only observable mononuclear rhodium intermediate and HML_n (M = Mn, Re, Mo, W) was the only observable mononuclear intermediate that contained the second metal.

$$r = [Rh(CO)_4RCO]^1[\text{alkene}]^0(k_\alpha[H_2]^1[CO]^{-1} + k_\beta[HML_n]^1[H_2]^0[CO]^{-1.6}) \tag{3}$$

The linear−bilinear Rh−Mn and Rh−Re hydroformylation reactions of alkenes have now been studied for more than a decade. A large variety of experimental techniques have been applied to better understand the functional form of the product rate in eq 3. Multiple-isotope labeling studies have conclusively shown that the bilinear term $[RhCO_4RCO][HML_n]$ arises from the bimolecular reaction between these 2 intermediates, and the term "catalytic binuclear elimination reaction" (CBER) has now been accepted to describe such systems.[44] In the case of the Rh−Re system,[36] the dinuclear species formed $RhRe(CO)_9$, which has been shown to exhibit extraordinary hydrogen activation kinetics.[45] Therefore it is not involved in the rate-limiting step and, hence, does not contribute to any kinetic expressions for the reaction. The extraordinarily unusual exponent of −1.5 for CO in the bilinear term is highly reproducible (variation of circa ±0.1). Such an unusual exponent suggests that something dramatically new is occurring in this bimetallic system and that one or more previously undocumented mechanisms/phenomena must be present. Thus, the present contribution will focus exclusively on the identified rate-controlling steps to shed light on these unusual kinetics.

The bilinear term, particularly in the case of Rh−Re hydroformylation, is responsible for most product formation. Moreover, the full expression demonstrates that the hydride $HReL_n$ (L = CO) was substantially more reactive than molecular hydrogen in the reaction with $Rh(CO)_4RCO$.

DOI: 10.1021/cs5019925
ACS Catal. 2015, 5, 2301−2316

Because $HRe(CO)_5$ shows no hydroformylation activity on its own[36] and with virtually all experimental avenues to investigate further exhausted, a combined approach using free energy surface (FES) scanning with density functional theory (DFT) and complementing molecular dynamics (MD) simulations was applied. In the present contribution, these two molecular simulation approaches were successfully used to identify the new and unusual reaction mechanism underlying heterobimetallic Rh−M catalytic binuclear elimination: The well-studied mononuclear hydroformylation reaction catalyzed with $Rh(CO)_4RCO$ and H_2 was studied as a reference system in the first step to provide a comparison with previously reported computational studies. After a successful validation of the DFT method, various catalytic reaction pathways for bimetallic hydroformylation with $HRe(CO)_5$ were identified and characterized. For the CBER, three interlocking catalytic cycles were identified in the reaction system. Moreover, MD simulations were used to observe a rapid aggregation of $Rh(CO)_4RCO$ and $HRe(CO)_5$ in the solvent, which is an essential process to initiate the subsequent reaction. The underlying cause of this aggregation was revealed, and the corresponding association free energy was derived to determine the extent of aggregation in solution. Finally, on the basis of these results, the functional form of eq 3 with all its salient features was successfully derived through kinetic analysis.

2. METHODOLOGY

2.1. Finding Reaction Pathways and Free Energy Profiles. *2.1.1. Specification of DFT Model.* All quantum chemical simulations were performed using Gaussian 09 Rev. A.1.[46] Considered compounds are described with DFT using the functionals from Becke and Perdew (BP86).[47,48] For all calculations, the extensive Pople triple-ζ basis set 6-311++G(d,p) was used, including polarization functions and diffuse functions on all atoms.[49] Core electrons of the heavy transition metals Rh and Re were treated with an effective core pseudopotential (ECP) from Andrae et al. (SDD option in Gaussian) to improve computational efficiency.[50] For the two observable compounds $Rh(CO)_4RCO$ and $HRe(CO)_5$, the sensitivity of the charge distribution with respect to the choice of the ECP was assessed by comparing the vibrational spectra calculated with the ECP from Andrae et al. and the ECP from Hay and Wadt (LanL2DZ option in Gaussian).[51] No significant deviations were found; only a maximum deviation of $\Delta\nu_{max} < 12\ cm^{-1}$ and a root-mean-square deviation (rmsd) of only 4.2 cm^{-1} were obtained, thus confirming that the DFT results for rhodium and rhenium carbonyl compounds are not sensitive to the particular choice of the ECP.

The potential energies of ground states (GS) and transition states (TS), which were determined from geometry optimizations, were corrected to include zero-point energies derived from a subsequent harmonic normal-mode analysis. Moreover, optimized GS and TS structures were evaluated with a polarizable continuum model (IEFPCM) in a single-point calculation using a dielectric constant of $\varepsilon_r = 1.88$ to describe solvation in hexane.[52] Thus, free energies of GS and TS in hexane that approximately take into account solute−solvent interactions, solvent cage formation, and entropic effects were determined. Nevertheless, we like to point out that solvent effects of nonpolar hexane on metal−carbonyls are generally weak as a result of limited mutual interactions, as demonstrated also in this work. Thus, the effect of the solvent on the structures of the metal carbonyls, which were optimized in vacuum, was neglected. Inclusion of thermal gas-phase corrections were deliberately avoided because of their limited applicability to solutions.

Counterpoise corrections to correct basis set superposition errors (BSSE) were not carried out intentionally.[53] There have been numerous indications recently that such corrections are problematic and are often not expected to improve the results but, rather, decrease accuracy, especially when close to TS on the potential energy surface where one would actually expect the largest BSSE.[54,55] The best way to mitigate the BSSE is, instead, the use of a sufficiently large basis set as a comparison with high accuracy CCSD(T) calculations clearly revealed.[55] Therefore, we omitted a BSSE correction for our systems, considering the fairly large size of the chosen basis set. See also comments in Papajak and Truhlar in ref 56.

The error of used basis set and density functional was assessed by calculating free energies of selected ground states and transition states using the larger correlation consistent triple-ζ basis set Aug-cc-pVTZ, the alternative functional PBE, the hybrid functional B3LYP, the dispersion corrected functional B97D3 and the ab initio method MP2.[57−63]

2.1.2. Determining Free Energy Surfaces. Free energy surfaces, $G(R)$, were determined as functions of selected reaction coordinates, R_i. During geometry optimizations, these R_i were constrained to different values, thereby effectively scanning the FES. GS could be located readily as minima on these FES with possible reaction paths connecting these minima. The path that passes through the lowest maximum energy defines the most probable reaction path, where the structure that corresponds to the point of maximum energy is the corresponding TS of the reaction. That GSs and TSs on the FES were found was confirmed by subsequently calculating the normal modes of these states. In the case of TSs, it was checked whether the normal amplitude with the imaginary vibrational frequency was, indeed, pointing into the direction of the expected reaction pathway.

Geometry optimizations were started from different initial structures at various points, R, to mitigate the well-known problem of initialization dependency of the energy minimization result. Only the structures of lowest energy were considered for assembling the overall effective FES. Crucial are the choices of R_i, whose definitions were adapted to describe the respective reaction steps effectively. It is essential to ensure that molecular structures that correspond to two neighboring points on the reaction pathway do not differ substantially in structure. In cases that such sudden conformational changes were noticed, additional R_i were introduced to describe these structural changes with additional FES scans. As a result, the overall reaction path connects reactants and products smoothly without involving molecular structural or energetic discontinuities along the path. All presented FESs in this work are described by either one or two reaction coordinates. The described approach of FES scanning resembles the method described in our previous work on phosphate hydrolysis (Warshel et al., ref 64).

2.2. Study of Binuclear Complex Formation with MD Simulation. *2.2.1. Specifications of MD Simulations.* All MD simulations were performed with the software GROMACS 4.5.5 using empirical force fields.[65−68] Standard force fields for rhodium and rhenium complexes are not available. Therefore, we performed a complete force field parametrization of the compounds $Rh(CO)_4RCO$ and $HRe(CO)_5$ through approximating the DFT model of these compounds as described in

DOI: 10.1021/cs5019925
ACS Catal. 2015, 5, 2301−2316

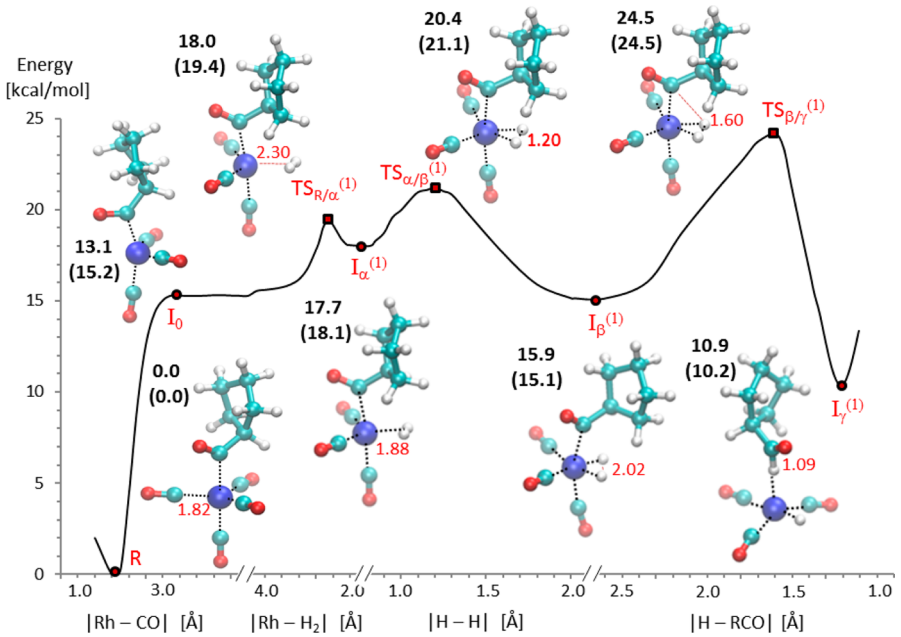

Figure 1. FES from relaxed scan of the H_2-catalyzed reaction $Rh(CO)_4RCO + H_2 \leftrightarrow HRh(CO)_3 + RCHO + CO$. The displayed potential was derived directly from FES scanning. The FES is a function of the distance between rhodium and carbon of the released carbonyl in the first step, |Rh−CO|; of the distance between rhodium and H_2 in the second step, |Rh−H_2|; of the distance between the two hydrogens in the third step, |H−H|; and of the distance between the transferred hydrogen and the carbon of the RCO acyl group in the last step, |H−RCO|. Structures of ground states and transition states are displayed together with their free energies in black and their potential energies in parentheses. Metalorganic bonds are indicated as dotted lines. Some critical reaction coordinate values for the indentified states are given in red. Structure abbreviations are summarized in Table 1.

section 2.2.1 as closely as possible. The full parametrization procedure and the derived force field parameters are described in the Supporting Information. For the solvent, hexane and the R = cyclopentyl ligand the OPLS-aa force field was used.[69,70]

One molecule of $Rh(CO)_4RCO$ and $HRe(CO)_5$ each were solvated together in a cubic box of about 4.9 nm box length and filled with 529 hexane solvent molecules, approaching the limit of infinite dilution. Full periodic boundary conditions were used. Simulations contained 10 637 atoms that were all treated explicitly. After an initial relaxation of the potential energy, the solution was simulated for 20 ns, in which eight replicas with different initial structures were used. A time step of 2 fs was used, together with constraints on bonds that involved hydrogen using the LINCS method.[71] Simulated was an isothermal−isobaric (NPT) ensemble at 290 K temperature and 4 MPa pressure, according to conditions used in our previous experiments.[36] Temperature and pressure of the simulations were controlled with a velocity rescaling thermostat and a Berendsen barostat, using coupling constants of 0.1 and 5 ps, respectively.[72,73] Electrostatic and Lennard-Jones interactions were treated explicitly up to atom pair distances of 1.5 and 1.0 nm, respectively. Beyond these cutoff distances, long-range electrostatics were evaluated with the fast particle-mesh Ewald (PME) method in combination with dispersion energy corrections.[74,75] Systems were found to be equilibrated after about 1 ns. The last 10 ns of the simulations were used for analysis.

2.2.2. Calculation of Free Energy of Association. Starting from an equilibrated solution of $Rh(CO)_4RCO \cdot HRe(CO)_5$ in hexane, in which both metal carbonyls formed a complex through nonchemical association, an additional harmonic potential with a force constant of 1000 kJ mol^{-1} nm^{-2} was applied as a function of the rhodium−rhenium distance, ξ. The minimum of this potential was gradually shifted by 1.6×10^{-3} nm ps^{-1} toward larger distances, ξ, during an MD simulation of 1 ns length, thereby effectively separating the two compounds adiabatically from a starting value of 0.4 to 2.6 nm. Subsequently, 11 structures from this simulation were singled out with specific values of ξ starting at 0.6 nm, with increments of $\Delta\xi$ = 0.2 nm, up to a maximum separation of 2.6 nm. These structures were used as starting points for 11 umbrella sampling simulations, respectively, in which ξ was restrained to the initial value with a force constant of 1000 kJ mol^{-1} nm^{-2}. The simulations were performed using the same MD parameters as discussed in the previous section. Simulation lengths were 5 ns for each ξ window, resulting in a total simulation length of 55 ns. That the separation of $\Delta\xi$ = 0.2 nm was sufficiently small was confirmed by observing substantial overlap of the ξ-value distributions between umbrella sampling simulations of neighboring ξ windows. Thus, the entire range of ξ values was sufficiently sampled, as shown in Figure S6. The pulling forces were written out for each ξ window, using only the last 4 ns for analysis, respectively. From these forces, the potential of mean force was derived by applying the weighted histogram analysis method.[76] From the resulting free energy function, $G(\xi)$, the free energy of association of $Rh(CO)_4RCO$ and $HRe(CO)_5$ could be determined as the free energy difference between the minimum at small ξ, that is, the associated state, and the value at large ξ, when the two compounds were fully separated from each other and solvated in hexane. The statistical error of free energies was calculated with the Bootstrap method.[77]

3. RESULTS

3.1. Mononuclear Hydroformylation with Rhodium−Carbonyl and H_2. In the first part, we studied the rate-limiting

DOI: 10.1021/cs5019925
ACS Catal. 2015, 5, 2301−2316

hydrogenolysis step of the *mononuclear* rhodium−catalyzed hydroformylation of cyclopentene involving H_2:

$$Rh(CO)_4RCO + H_2 \leftrightarrow HRh(CO)_3 + RCHO + CO \quad (4)$$

R in eq 4 designates, in our case, cyclopentyl. Analysis of this reaction serves two purposes: (1) enabling a direct comparison with other computational work of the same reaction to verify the applied method and (2) providing a reference reaction for *binuclear* hydroformylation to characterize and to find the underlying origin of the observed enhanced heterobimetallic catalysis.

All identified GSs and TSs, together with the calculated FES for this reaction, are given in Figure 1. Energies of all identified states are listed in Table S4. On the calculated FES, these found structures are abbreviated using the designations given in Table 1. The reaction starts with the most stable and also

Table 1. Abbreviations of Reaction States

abbreviation	compd (R = cyclopentyl)
R	$Rh(CO)_4RCO$
$\mathbf{I_0}$	$Rh(CO)_3RCO$
$\mathbf{I_\alpha^{(1)}}$	$Rh(CO)_3RCO{\cdot}H_2$
$\mathbf{I_\beta^{(1)}}$	$H_2Rh(CO)_3RCO$
$\mathbf{I_\gamma^{(1)}}$	$HRh(CO)_3{\cdot}RCHO$
$\mathbf{P^{(1)}}$	$HRh(CO)_3$
$\mathbf{I_\alpha^{(2)}}$ / $\mathbf{I_\alpha^{(3)}}$	$Rh(CO)_3RCO{\cdot}HRe(CO)_5$
$\mathbf{I_\beta^{(2)}}$	$HRhRe(CO)_8RCO$
$\mathbf{I_\gamma^{(2)}}$	$RhRe(CO)_8{\cdot}RCHO$
$\mathbf{P_1^{(2)}}$	$RhRe(CO)_8$
$\mathbf{P_2^{(2)}}$	$RhRe(CO)_9$
$\mathbf{I_2^{(3)}}$	$Rh(CO)_3R{\cdot}HRe(CO)_5$
$\mathbf{I_3^{(3)}}$	$Rh(CO)_2RCO{\cdot}HRe(CO)_5$
$\mathbf{I_1^{(4)}}$	$Rh(CO)_4R$

spectroscopically well observed and characterized ground state of the coordinatively saturated rhodium complex, $Rh(CO)_4RCO$.[36] Rhodium, carbonyl, and RCO form a trigonal−bipyramidial structure, with Rh in the center, where three carbonyl are spanning the equatorial plane, and one carbonyl and RCO occupy opposing axial positions (see, e.g., ref 78). In the first reaction step, rhodium is activated by dissociation of one equatorial carbonyl and oxidative addition of H_2, which provides the hydrogen for the hydrogenolysis step. The loss of one carbonyl and addition of H_2 has been repeatedly confirmed by the measured hydroformylation product formation rate that was found to be proportional to $[CO]^{-1}{\cdot}[H_2]$.[36] This observation also shows that the rate-limiting step is, indeed, the hydrogenolysis step. For binding H_2, rhodium needs to be activated first by dissociating one carbonyl. It has not been clear whether this exchange proceeds in a stepwise manner, in which carbonyl is released first before subsequent H_2 binding, or concerted with a transition state in which leaving carbonyl and approaching H_2 are at similar distances from rhodium. Both a stepwise and a concerted mechanism would reproduce the observed reaction order. For this reason, we determined the FES as a function of two reaction coordinates: namely, the distances of Rh−CO and of Rh− H_2. The result is shown in Figure 2.

According to this FES, the intermediate $\mathbf{I_\alpha^{(1)}}$ was found, in which one of the equatorial carbonyls was exchanged by H_2, which occupied the place of the dissociated carbonyl in the

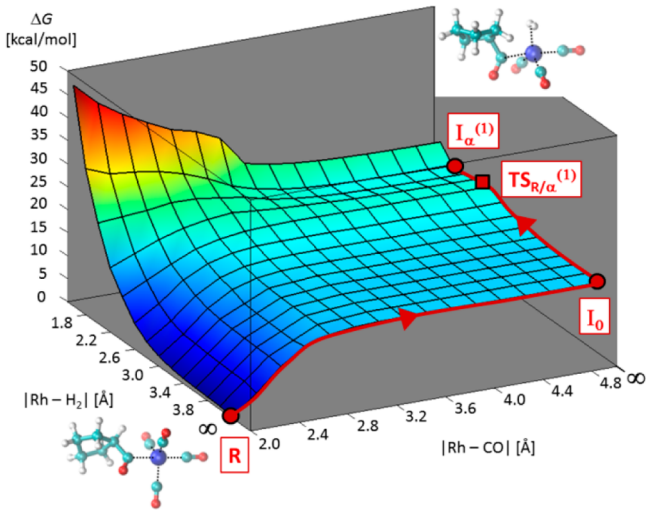

Figure 2. FES from relaxed scan of first step in H_2-catalyzed reaction: $Rh(CO)_4RCO + H_2 \leftrightarrow Rh(CO)_3RCO{\cdot}H_2 + CO$. The FES is a function of the two reaction coordinates |Rh−CO|; the distance between rhodium and carbon of the dissociating CO ligand; and |Rh−H_2|, the distance between rhodium and H_2. Large values of |Rh−CO| and |Rh−H_2| at the FES edges correspond to infinite distance of the compounds. Ground states and transition state as well as the connecting reaction path are indicated on the FES in red with abbreviations given in Table 1

complex. The H_2 bond was oriented in parallel to the equatorial ligand plane of rhodium, with both hydrogen atoms at equal distance of 1.88 Å to Rh (see Figure 1). Release of the axial carbonyl opposite to RCO was also investigated; however, the related energy barrier was found to be substantially larger compared with the release of an equatorial carbonyl, as shown in Figure S7. The three equatorial CO's are essentially equivalent because the interactions of the axial cyclopentane carboxaldehyde ligand with the other parts of the rhodium complex are negligible, as shown in Figure S8. To reach the intermediate $\mathbf{I_\alpha^{(1)}}$, an energy barrier parallel to the direction of the Rh−CO distance needs to be crossed. The barrier height appeared to be insensitive to the particular value of the Rh−CO distance. Nevertheless, the barrier slowly decreased with increasing Rh−CO distance, leading to a transition state $\mathbf{TS_{R/\alpha}^{(1)}}$ at full dissociation of CO, that is, characteristic for a stepwise reaction that proceeds via $\mathbf{I_0}$, the activated rhodium complex $Rh(CO)_3RCO$. The corresponding free energy barrier was 18.0 kcal/mol at a distance of 2.30 Å between H_2 and rhodium. A concerted reaction pathway was not found on the FES. Because of the proximity of the intermediate $\mathbf{I_\alpha^{(1)}}$ to the TS, the energy of $\mathbf{I_\alpha^{(1)}}$ of 17.7 kcal/mol was only 0.3 kcal/mol lower than the TS energy, that is, thermal energy would be sufficient to enable the back reaction. This suggests that this intermediate is highly unstable.

In the second step of the reaction. the homolytic H_2-bond breaks. The corresponding FES as a function of the H−H bond length is shown in Figure 1. A second intermediate, $\mathbf{I_\beta^{(1)}}$, was found, in which the H_2 bond was broken and two carbonyl ligands together with the two separated hydrogen atoms spanned the equatorial ligand plane with rhodium in the center. The distance of hydrogen atoms to Rh was 1.60 Å. The free energy barrier crossing the transition state, $\mathbf{TS_{\alpha/\beta}^{(1)}}$, starting from $\mathbf{I_\alpha^{(1)}}$ was found to be only 2.7 kcal/mol, after which the energy decreased to 15.9 kcal/mol. Given the similarity of $\mathbf{TS_{R/\alpha}^{(1)}}$ and $\mathbf{I_\alpha^{(1)}}$, it is reasonable to combine the first two steps

DOI: 10.1021/cs5019925
ACS Catal. 2015, 5, 2301−2316

from the ground state R to $\mathbf{I}_{\beta}^{(1)}$ into one step that exhibits an overall activation free energy of 20.4 kcal/mol. However, it will be more instructive to describe the reaction with three separate steps, which will become clearer in later sections when we compare mononuclear and binuclear reactions.

In the third step, one of the hydrogen atoms is internally transferred from rhodium to the acyl carbon bonded to cyclopentyl. The FES as a function of the H−C(RCO) distance is also shown in Figure 1. With the third intermediate, $\mathbf{I}_{\gamma}^{(1)}$, the hydrogen transfer was completed, and the formed product of the reaction, RCHO, remained bonded to rhodium through the transferred hydrogen. Crossing the involved transition state, $\mathbf{TS}_{\beta/\gamma}^{(1)}$, from $\mathbf{I}_{\beta}^{(1)}$ required overcoming a barrier of 8.6 kcal/mol. The state $\mathbf{I}_{\gamma}^{(1)}$ exhibited a favorable energy of 10.8 kcal/mol. In the last step, in which the hydroformylation product RCHO, $\mathbf{P}^{(1)}$, is released, the energy increased slightly, by 2.2 kcal/mol, as a result of the cleavage of the weak Rh−H bond.

Overall, the largest single activation barrier to overcome for this reaction was related to the activation of the rhodium complex by releasing one carbonyl in combination with the binding of H_2. To determine the overall activation barrier of the reaction cycle, we used the method of turnover-determining states from Kozuch and Shaik with the approximation of one influential transition state and intermediate.[79,80] The rate-determining states are $\mathbf{TS}_{\beta/\gamma}^{(1)}$ and **R**, resulting in a free energy span of 24.5 kcal/mol.

The energies of all occurring states are summarized in Table S4. Solvation free energies were generally found to be small. This is not surprising because hexane is a nonpolar solvent with a dielectric constant of only ε_r = 1.88. The solvation of H_2, carbonyl, and $HRh(CO)_3$ were found to be only 0.0, −0.2, and −0.6 kcal/mol, respectively. Solvation of the acyl group led to slightly larger solvation free energies of −1.1 kcal/mol for $Rh(CO)_4RCO$ and RCHO.

The results of this reaction could be compared quantitatively with other computational studies. In the study from Gleich and Hutter, the complete reaction cycle of rhodium−carbonyl catalyzed hydroformylation of ethene was studied with DFT, in which the same BP86 functional was used that was also applied in this work, thus enabling a direct comparison.[81] Because neither ethene nor cyclopentene is directly involved in the reaction steps discussed here, a comparison should not be compromised. All eight different intermediates and TS that occurred during carbonyl migratory insertion (as discussed in section 3.4) and during hydrogenolysis (as discussed in this section) were the same as those identified in this work. A direct comparison of calculated energies of these states derived in this work and given in ref 81 yielded a rmsd value of only 1.0 kcal/mol. Calculated activation barriers for carbonyl migratory insertion and hydrogenolysis were found in ref 81 to be 15 and 20 kcal/mol, respectively, which compare to 13 and 20 kcal/mol found in this work. Therefore, the results of these two studies are in very good agreement.

In the more recent work from Sparta et al., the complete reaction cycle of the same reaction was studied with DFT using the hybrid functionals O3LYP and B3LYP.[78] As before, the same eight states for carbonyl migratory insertion and hydrogenolysis were found, including the ground state, **R**, as the ninth state that was not considered in ref 81. Solvent corrected potential energies that were provided as Supporting Information in ref 79 enabled a direct comparison with values in this work. Inclusion of gas-phase thermal corrections to energies was avoided in this work, as discussed in section 2.1. We found a rmsd of 2.5 kcal/mol compared with our values, which is within the range of what is to be expected for using different DFT functionals, as will be demonstrated also in section 3.3 of this work. Barriers in ref 78 for carbonyl migratory insertion and hydrogenolysis were found to be 15 and 18 kcal/mol, respectively, in comparison with 13 and 20 kcal/mol in this work. Overall, calculated energies agree well, considering the use of different DFT functionals.

Hydroformylation reactions catalyzed by various other organometallic complexes, in particular cobalt complexes, that exhibit characteristics similar to the case considered in this section have been extensively studied.[82] A comparison of intermediates and TS structures for instance for the hydroformylation of ethylene with $HCo(CO)_3$ was found to be quite similar to the structures identified in this study.[83]

Overall, the comparison with other computational work corroborates our findings. Hence, we proceeded to apply confidently the same methodology to describe the binuclear hydroformylation reaction in the following sections.

3.2. Association of Rhodium and Rhenium Complexes in Solution. Before we studied binuclear chemical reactions of rhodium and rhenium complexes, we explored the possibility of nonchemical aggregation, that is, association, of these two metal complexes. Considering the trace amounts of rhenium that are sufficient to catalyze hydroformylation according to experiments, the question arises how likely an encounter of these two metals in solution even is, especially considering that other potential reaction partners for rhodium, such as CO and H_2, are present in considerably larger quantity. Therefore, we studied the rhodium complex $Rh(CO)_4RCO$ together with $HRe(CO)_5$ solvated in hexane with MD simulations at a temperature of 290 K and a pressure of 4 MPa according to our previously reported experimental conditions. Both compounds have been spectroscopically clearly identified in the bimetallic hydroformylation reaction. In simulations, only one rhodium and one rhenium complex were added to 529 hexane solvent molecules. Eight replicas of these systems were simulated.

We observed in all simulations that rhenium readily approached the rhodium complex, after which it remained in its vicinity throughout most of the remaining simulations. The radial distribution functions (RDF) of rhodium−rhenium pairs as well as of rhodium−hydrogen pairs were derived from simulations and are shown in Figure 3. A distinctive peak with a maximum at a rhodium−rhenium distance of 6.7 Å was observed, indicating that both complexes were associated throughout most of the simulations. Furthermore, two peaks of the RDF at rhodium−hydrogen distances of 5.2 and 7.8 Å, respectively, were found. These two peaks corresponded to two different orientations of $HRe(CO)_5$ relative to the rhodium complex, with either axial hydrogen or axial carbonyl pointing toward rhodium. Two examples were taken from MD simulations and are displayed in Figure 3, together with the RDFs. It was remarkable that hydrogen could readily approach rhodium as close as 4 Å or even less, a distance at which a reaction involving hydrogen transfer from rhenium to rhodium could easily occur during the association of the two metal complexes, as will be shown in sections 3.3 and 3.4.

From the final structures of the eight replicas, MD simulations were continued with a combined quantum mechanical/molecular mechanical (QM/MM) force field, in which the rhodium and rhenium complexes were described with DFT, whereas the solvent was treated with the MM force field. Details of the QM/MM method are described in the

DOI: 10.1021/cs5019925
ACS Catal. 2015, 5, 2301−2316

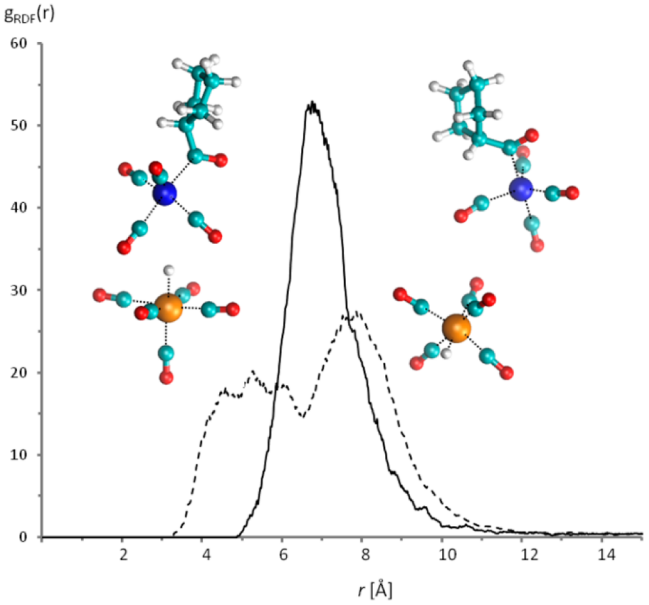

Figure 3. Radial distribution functions, g_{RDF}, of rhodium−rhenium distances (straight line) and rhodium−hydrogen distances (broken line) derived from MD simulations of $Rh(CO)_4RCO$ and $HRe(CO)_5$ at T = 290 K and P = 40 MPa solvated in hexane. A distinct peak with a maximum at 6.7 Å of rhodium−rhenium distance indicates association of the two complexes. The two peaks with maxima at ∼5 and 8 Å of rhodium−hydrogen distance correspond to orientations of $HRe(CO)_5$ with H pointing toward rhodium or with axial carbonyl pointing toward rhodium, respectively. Two structures taken from MD simulations that represent these two $HRe(CO)_5$ orientations are displayed.

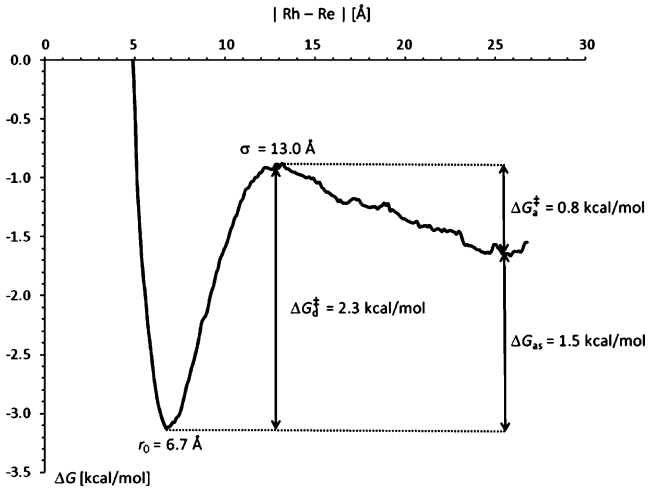

Figure 4. Free energy profile of the nonchemical aggregation of the two complexes $Rh(CO)_4RCO$ and $HRe(CO)_5$ as a function of the rhodium−rhenium distance. The association free energy is ΔG_{as} = 1.5 kcal/mol, with a ground state association distance of r_0 = 6.7 Å. Dissociation occurs at σ = 13.0 Å after overcoming a free energy barrier of $\Delta G_d^{\ddagger}$ = 2.3 kcal/mol. The free energy barrier for enabling association is $\Delta G_a^{\ddagger}$ = 0.8 kcal/mol.

Supporting Information. The 1 ps long trajectories were too short to observe any chemical reactions; however, we observed that previously found structures did not change significantly upon switching from a pure MM to a QM/MM force field and that associated rhodium−rhenium complexes remained stable. This finding confirmed that the results of classical MD simulation indeed closely resembled a DFT description of these systems, which enhanced confidence in the simulations further.

In the next step, we derived the association free energy, ΔG_{as}, through thermodynamic integration, as described in subsection 2.2.2. The free energy profile is shown in Figure 4 as a function of the rhodium−rhenium distance, which was increased in a stepwise manner until full dissociation was achieved. The value of ΔG_{as} was determined as 1.5 kcal/mol, that is, the complexes of rhodium and rhenium were only weakly associated. The free energy barrier for association to form, $\Delta G_a^{\ddagger}$, was only 0.8 kcal/mol, and for dissociation, the involved energy barrier, $\Delta G_d^{\ddagger}$, was 2.3 kcal/mol. Thus, association could be readily accomplished with the available thermal energy while dissociation was impeded, which gave rise to the observed weak association of rhodium and rhenium complexes in simulations. The energetically most favorable rhodium−rhenium distance was 6.7 Å in the associated state, whereas beyond σ = 13.0 Å, full dissociation occurred. This distance, σ, is essentially the maximum distance within which rhodium and rhenium complexes are effectively attracted toward each other.

With ΔG_{as}, the fraction of rhodium complexes that are associated with rhenium can be determined from the initial concentrations of $Rh(CO)_4RCO$ and $HRe(CO)_5$. The relations are described in the Supporting Information in eqs S2−S6.

According to ref 36 (Figure 2 therein) typical values for initial $Rh(CO)_4RCO$ and $HRe(CO)_5$ concentrations are, for example, 4.6×10^{-4} M and 3.0×10^{-4} M, respectively, which gives an equilibrium concentration for rhodium−rhenium association, $[RhRe]_{equ}$, of 1.73×10^{-6} M according to eqs S5 and S6. That means that ∼0.4% of all $Rh(CO)_4RCO$ compounds are associated with $HRe(CO)_5$ at each time. Compared with a case in which effective attraction between rhodium and rhenium complexes is absent, that is, wherein eq S6 ΔG_{as} = 0 so that the rhenium concentration around rhodium is merely based on the homogeneous rhenium concentration in the solution, the number of associated complexes formed increased by a factor of 12.7. For binuclear hydroformylation to proceed, the formation of such associated rhodium−rhenium complexes is an essential initial step. Furthermore, the production rate for hydroformylation is proportional to the rhenium concentration. Therefore, because the calculated association free energy caused a local increase of rhenium concentration by a factor of 12.7 around rhodium, the production rate, which depends linearly on the rhenium concentration, should consequently increase by the same factor. Or expressed differently, an acceleration of product formation due to an increase in the reactant concentration by a factor of 12.7 is equivalent to an effective decrease in the activation free energy by 1.5 kcal/mol. We will show in the next sections that rhenium lowers the effective activation barrier of hydroformylation by 5.7 kcal/mol compared with mononuclear hydroformylation; that is, nonchemical rhodium−rhenium association appears to be a significant secondary effect that contributes to enhanced catalysis.

The remaining question was how the observed rhodium−rhenium attraction is caused. Hence, we determined average interaction strengths of the rhenium and rhodium complexes with each other and with the hexane solvent from MD simulations. These interaction strengths were evaluated at average rhodium−rhenium distances of 6 Å, that is, the most probable distance of rhodium and rhenium when associated, and 26 Å, respectively, by applying a harmonic restraint to this

DOI: 10.1021/cs5019925
ACS Catal. 2015, 5, 2301−2316

distance. The results are listed in Table 2, where individual contributions from electrostatic and van der Waals interactions

Table 2. Interaction Energy Strengths in MD Simulations of $Rh(CO)_4RCO$ and $HRe(CO)_5$ Solvated in Hexane[a,b,c]

	Hex−Hex	Rh−Hex	Re−Hex	Rh−Re
		|Rh−Re| = 6 Å		
Coulomb	-916_1	0.0_1	0.0_1	-0.1_1
Lennard-Jones	-3819_1	-8.3_1	1.2_1	0.5_1
total	-4735_2	-8.3_1	1.2_1	0.4_1
		|Rh−Re| = 26 Å		
Coulomb	-917_1	0.0_1	0.0_1	0.0_1
Lennard-Jones	-3815_1	-8.2_1	1.7_1	0.0_1
total	-4732_2	-8.2_1	1.7_1	0.0_1

[a]Average interaction energies from MD simulations, with the rhodium−rhenium distance restrained with a harmonic potential to 6 and 26 Å, at T = 290 K and P = 4 MPa. [b]All energies are given in units of kcal/mol. [c]Statistical uncertainties evaluated with the block averaging method are given as subscripts.

are also given. The results surprisingly and clearly show that interactions between rhodium and rhenium complexes were negligible at all distances; therefore, the observed rhodium−rhenium attraction was not caused by direct interactions. Moreover, the interactions of rhenium complexes with the solvent also were negligible. Only a weak attractive van der Waals interaction with hexane was found for rhodium complexes, which stemmed mostly from interactions of cyclopentyl and not from the metal carbonyl part. The markedly weak metal−carbonyl interactions with hexane were a consequence of the previously obtained DFT potentials shown in Figure S3, where no attraction between metal carbonyls and alkyl groups were found. The MM force field parametrization was based on these potentials as discussed in the Supporting Information. In any event, these negligible interactions between solvent and metal complexes led to a solvophobic effect, in which the solution organized itself to minimize the surface area of the solute−solvent interface. This was achieved by forming solute aggregates to avoid unfavorable solute−solvent interactions. This also explains why rhenium complexes were always found in simulations close to rhodium−carbonyl rather than close to the nonpolar cyclopentyl ligand. Cyclopentyl interacted more favorably with nonpolar hexane and, thus, preferred to stay in contact with the solvent.

Overall, results from MD simulations indicated that a solvophobic effect caused association of rhenium and rhodium. This effect caused a great reduction of the average distance between rhodium and rhenium and furthermore facilitated an orientation of the rhenium complex, in which the hydrogen of $HRe(CO)_5$ was found in close proximity to rhodium to enable hydrogen transfer to the rhodium complex to enable the hydroformylation reaction. Even though not explicitly calculated, a similar enhanced association probability of $HRe(CO)_5$ with other less stable rhodium intermediates can be expected because of the same solvophobic effect.

3.3. Binuclear Hydroformylation with Rhenium−Carbonyl Complex. In this section, the enhanced catalysis of hydroformylation of cyclopentene with rhodium−carbonyl with addition of $HRe(CO)_5$ was analyzed. Starting points for rhodium and rhenium structures and their relative orientation were suggested by results from previous MD simulations, as discussed in the last section. This *binuclear* reaction that

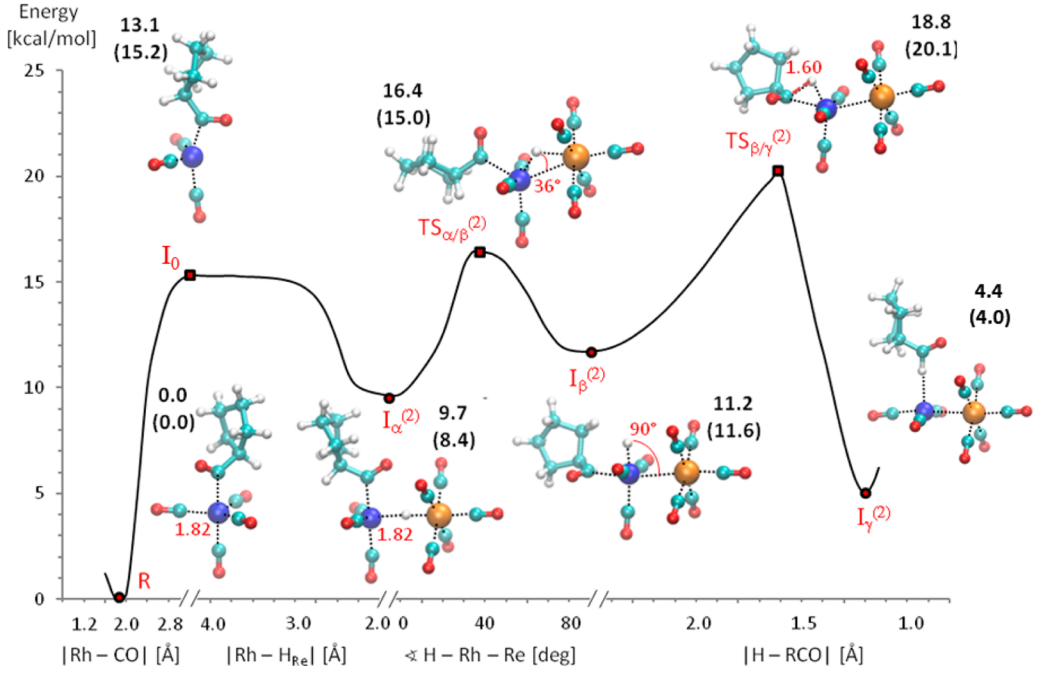

Figure 5. FES from a relaxed scan of the rhenium-catalyzed reaction $Rh(CO)_4RCO + HRe(CO)_5 \leftrightarrow RhRe(CO)_8 + RCHO + CO$. The displayed potential was derived directly from FES scanning. The FES is a function of the distance between rhodium and carbon of the released carbonyl in the first step, |Rh−CO|; of the distance between rhodium and the hydrogen of $HRe(CO)_5$ in the second step, $|Rh-H_{Re}|$; of the angle between hydrogen, rhodium, and rhenium in the third step, ∠|H−Rh−Re|; and of the distance between the transferred hydrogen and the carbon of the RCO acyl group in the last step, |H−RCO|. Structures of ground states and transition states are displayed, together with their free energies in black and their potential energies in parentheses. Metalorganic bonds are indicated as dotted lines. Some critical reaction coordinate values for the identified states are given in red. Structure abbreviations are summarized in Table 1

DOI: 10.1021/cs5019925
ACS Catal. 2015, 5, 2301−2316

involves a rhenium−carbonyl complex has been found to accelerate product formation substantially by a factor 5−10, depending on reaction conditions, even at very low concentrations of rhenium down to 10^{-5} M.[36] As in the case of mononuclear hydroformylation, the hydrogenolysis step was found to be rate-limiting in the same study. Therefore, we explored the FES of the following reaction in eq 5:

$$Rh(CO)_4RCO + HRe(CO)_5 \leftrightarrow RhRe(CO)_8 + RCHO + CO \quad (5)$$

While the transient coordinatively unsaturated bimetallic complex $RhRe(CO)_8$ is too unstable to be detected directly, it is in equilibrium with the saturated species $RhRe(CO)_9$, which was identified successfully with IR spectroscopy.[36]

Without prejudices regarding the reaction path, a FES connecting the reactant **R** and the product state was explored with different reaction coordinates. Structures of identified intermediates and TS are shown in Figure 5, and the corresponding energies are listed in Table S5. Abbreviations of states are given in Table 1. The energies of all states were measured relative to the state $Rh(CO)_4RCO$, that is, **R**, as before to enable a straightforward comparison with the energy reaction profile for the mononuclear case.

The structure of the second metal−carbonyl, $HRe(CO)_5$, is square bipyramidal, with rhenium in the center of one equatorial plane spanned by four carbonyls, and the other carbonyl and hydrogen are in opposing axial positions. Starting from orientations of $HRe(CO)_5$ relative to $Rh(CO)_4RCO$, as suggested by MD simulations, the FES was calculated as a function of the distances between rhodium and the hydrogen of the rhenium complex as well as the distance between rhodium and the leaving equatorial carbonyl group. In addition, other orientations of $HRe(CO)_5$ relative to the rhodium complex were considered; however, the reaction path leading to product formation involved exactly the $HRe(CO)_5$ orientation that was obtained from MD simulations.

The results are shown in Figure 6. As in the case of the mononuclear hydroformylation, two distinct reaction pathways could be identified: a stepwise reaction path in which hydrogen bonds to rhodium only after carbonyl was released and a concerted pathway in which carbonyl release and Rh−H bond formation occurred simultaneously. An intermediate, $\mathbf{I}_\alpha^{(2)}$, was identified in which after the dissociation of one equatorial carbonyl, hydrogen is equally shared between rhodium and rhenium, with bond distances of |H−Rh| = 1.83 Å and |H−Re| = 1.82 Å. The bond angle H−Rh−Re was found to be 9.6°, that is, the three atoms Rh, H, and Re were almost aligned in one straight line. FES scans starting from different orientations of $HRe(CO)_5$ always led to the same orientation, with hydrogen oriented toward rhodium at sufficiently short rhodium−rhenium distances to avoid steric clashes between the carbonyl groups of the two metals. A concerted reaction path was found that proceeded via the transition state $\mathbf{TS'}_{R/\alpha}^{(2)}$ at an energy of 16.1 kcal/mol. The stepwise reaction path involved full dissociation of one equatorial CO to form state $\mathbf{I}_0$, followed by barrierless binding of the rhenium complex to form state $\mathbf{I}_\alpha^{(2)}$ at 8.4 kcal/mol. $\mathbf{I}_0$ is the state of highest energy on this stepwise reaction path and is energetically more favorable than $\mathbf{TS'}_{R/\alpha}^{(2)}$ by 13.1 kcal/mol. Therefore, these results suggest that the full release of one carbonyl precedes the approach of $HRe(CO)_5$ to form the intermediate $\mathbf{I}_\alpha^{(2)}$.

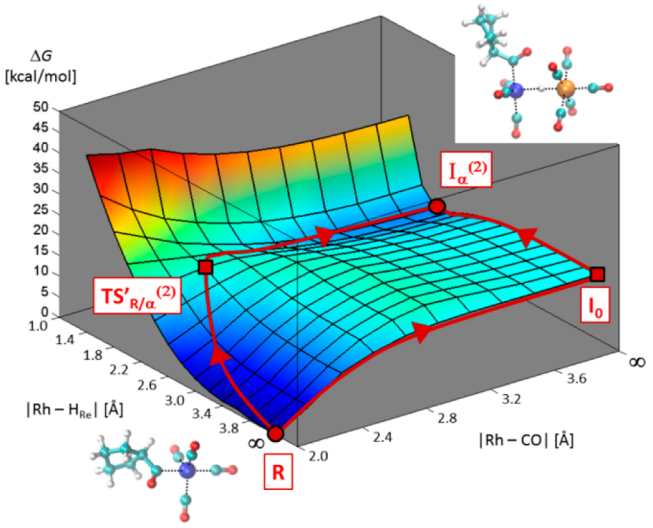

Figure 6. FES from relaxed scan of first step in the rhenium-catalyzed reaction: $Rh(CO)_4RCO + HRe(CO)_5 \rightarrow Rh(CO)_3RCO{\cdot}HRe(CO)_5 + CO$. The FES is a function of the two reaction coordinates |Rh−CO|; the distance between rhodium and carbon of the dissociating CO ligand, and $|Rh-H_{Re}|$; and the distance between rhodium and the hydrogen bonded to rhenium. Large values of |Rh−CO| and $|Rh-H_{Re}|$ at the FES edges correspond to infinite distance of the compounds. Ground states and transition states as well as connecting reaction paths are indicated on the FES in red with abbreviations given in Table 1. Both stepwise and concerted reaction pathways are highlighted on the FES. A comparison with the FES of the H_2-catalyzed reaction shown in Figure 2 clearly shows stabilization of $\mathbf{I}_\alpha^{(2)}$ compared with $\mathbf{I}_\alpha^{(1)}$.

In the next step, hydrogen was fully transferred from rhodium to rhenium. An adequate reaction coordinate to describe this process was found to be the bond angle formed by the atoms H−Rh−Re. The corresponding FES is shown in Figure 5. The value of the angle increased from almost linearity at $\mathbf{I}_\alpha^{(2)}$ (9.6°) to a right angle (90.5°) at newfound intermediate $\mathbf{I}_\beta^{(2)}$. During this reaction step, the bond between rhenium and hydrogen was cleaved, and a bond between rhodium and rhenium of 3.08 Å length emerged to generate a heterogeneous bimetallic Rh−Re compound. Furthermore, the RCO moiety moved to a new ligand position so that RCO and rhenium were in opposing positions, with rhodium in the center. This enabled hydrogen to fill the previous RCO position. The structure of $\mathbf{I}_\beta^{(2)}$ can be described with a parallel alignment of two equatorial planes centered on rhodium and rhenium. The three carbonyls and hydrogen formed the first equatorial plane around rhodium, and four other carbonyls formed the second equatorial plane around rhenium. RCO and Re were in axial positions of the first plane, and Rh and another carbonyl were in axial positions of the second plane. The activation free energy that had to be overcome was 6.6 kcal/mol. After passing the transition state $\mathbf{TS}_{\alpha/\beta}^{(2)}$, the energy decreased to 11.2 kcal/mol in $\mathbf{I}_\beta^{(2)}$.

In the third step, hydrogen was transferred to the carbon of the acyl group. The FES as a function of H−C(RCO) distance is included in Figure 5. In the new intermediate $\mathbf{I}_\gamma^{(2)}$ at 4.4 kcal/mol, hydrogen transfer was complete, whereas RCHO remained bonded to rhodium via hydrogen. Carbonyl coordinated to rhodium underwent reorganization, where the three carbonyl and rhodium form a plane perpendicular to the equatorial plane of rhenium. RCHO filled an axial position

DOI: 10.1021/cs5019925
ACS Catal. 2015, 5, 2301−2316

relative to that plane. The reaction free energy for this step was 7.6 kcal/mol.

In the last step, the weak hydrogen−rhodium bond was cleaved, which caused a slight energy increase of 0.8 kcal/mol to release the product RCHO. This unstable unsaturated state, $\mathbf{P_1}^{(2)}$, readily binds an additional carbonyl to form the observed complex $RhRe(CO)_9$, abbreviated here as $\mathbf{P_2}^{(2)}$, which was found to be 15.7 kcal/mol lower in energy than $\mathbf{P_1}^{(2)}$. The Rh−Re bond lengths were 2.93 and 3.05 Å in $\mathbf{P_1}^{(2)}$ and $\mathbf{P_2}^{(2)}$, respectively. In subsequent steps to complete the catalytic cycle, $RhRe(CO)_9$ dissociates one carbonyl and reacts with H_2 with the overall reaction $RhRe(CO)_9 + H_2 \leftrightarrow HRh(CO)_3 + HRe(CO)_5 + CO$. This part of the reaction is not rate-limiting and was thus not considered in this work.[36]

After finding the reaction mechanism, a comparison with the results from the mononuclear hydrogenolysis reaction were important to identify the catalytic effect of the rhenium complex. It was striking that for each intermediate in the mononuclear reaction, an analog intermediate was found in the binuclear reaction: in both cases, the transitions from **R** to $\mathbf{I}_\alpha^{(1)}$ and $\mathbf{I}_\alpha^{(2)}$ involved binding of the hydrogen-providing compound, that is, H_2 or $HRe(CO)_5$, to the rhodium complex. In the second step from $\mathbf{I}_\alpha^{(1)}$ to $\mathbf{I}_\beta^{(1)}$ and from $\mathbf{I}_\alpha^{(2)}$ to $\mathbf{I}_\beta^{(2)}$, cleaving the bond between hydrogen and the hydrogen-providing compound, that is, H−H or H−$Re(CO)_5$, was enabled by forming bonds between hydrogen and electron-rich rhodium instead, that is, Rh−H or Rh−Re. In both cases, in the third step, the hydrogen was then finally transferred from rhodium to the acyl group, states $\mathbf{I}_\gamma^{(1)}$ and $\mathbf{I}_\gamma^{(2)}$. We like to point out that reaction coordinates were not chosen intentionally so as to find an analogy between the mononuclear and binuclear reaction,; that is, the found similarities were not invested a-priori into our simulations. In fact, various other reaction coordinates have been tested, among them also a coordinate describing direct transfer of hydrogen from rhenium to cyclopentanecarbonyl. Only those reaction coordinates that successfully connected the reactant with product state are reported here. In fact, when one hydrogen in H_2 is replaced by $Re(CO)_5$ in the structures shown in Figure 1 for the mononuclear case, the resulting structures would resemble the structures displayed in Figure 5 for the binuclear case.

For both mononuclear and binuclear hydroformylation, the single reaction step with the largest activation energy was found to be the first step from **R** to $\mathbf{I}_\alpha^{(1)}$ and $\mathbf{I}_\alpha^{(2)}$. Comparing the corresponding FESs in Figures 2 and 6 shows clearly a stabilization of the first intermediate $\mathbf{I}_\alpha^{(2)}$compared with $\mathbf{I}_\alpha^{(1)}$, which was found to be 9.3 kcal/mol lower in energy. Together with a stabilization of the α-state, the energy of the preceding state of highest energy, that is, $\mathbf{I_0}$, was lower compared with $\mathbf{TS}_{R/\alpha}^{(1)}$ by 4.9 kcal/mol. A direct comparison of the FESs for all subsequent steps, as shown in Figure S9, indicated that the FES for the transitions from the α-state to the γ-state for the binuclear case is more or less congruent with the FES of the mononuclear case but shifted toward lower energies. This indicates a general stabilization of the rhodium−rhenium complex compared with the rhodium-H_2 complex. Such a stabilization could be induced by electron-rich rhenium, in which a redistribution of electrons would facilitate a saturation of the rhodium complex after release of one carbonyl. In the case of H_2 with only two tightly bonded electrons, such a saturation of rhodium is much more difficult to accomplish. In any event, barriers from the α-state to the β-state and from the β-state to the γ-state were less affected by the addition of rhenium than the barrier for the first reaction step. Overall, the energy span of the entire reaction is given by the rate-determining states $\mathbf{TS}_{\beta/\gamma}^{(2)}$ and **R**, in analogy to the mononuclear case. The free energy span is 18.8 kcal/mol, as compared with 24.5 kcal/mol for mononuclear hydroformylation. From this, we derived an overall catalytic effect for $HRe(CO)_5$ of $\Delta\Delta G^{\ddagger} = -5.7$ kcal/mol due to a stabilization of the rhodium−rhenium complex compared with a complex of rhodium and H_2.

These calculated free energy barriers can be compared with measured activation free energies. From the measured rate constants of $k = 0.33$ min^{-1} for mononuclear hydroformylation and $k = 110$ min^{-1} (see ref 36) at $T = 290$ K, for the same reactions that were considered here, activation free energies can be estimated by applying the Eyring equation, eq 6:

$$k = f_t \frac{k_B T}{h} e^{-\Delta G^{\ddagger}/k_B T} \tag{6}$$

With a transmission coefficient of $f_t = 1$, the measured rate constants translate to activation free energies of 20.0 and 16.6 kcal/mol for mononuclear and binuclear reactions, respectively, which should be compared with the free energy spans that we determined before.[80] This means that the calculated barriers are in good agreement with measured values. Although the activation energy for mononuclear hydrolysis is somewhat overestimated, but within the expected accuracy of DFT, the calculated barrier for the binuclear case is close to the measured value. Especially the catalytic effect is reproduced quite well.

At this point, it is important to establish the error of the DFT method that we used. For all ground states and TS that were identified in this section and in 3.1, calculations were repeated using the larger correlation-consistent triple-ζ basis set Aug-cc-pVTZ, the functional PBE, the hybrid functional B3LYP, the dispersion-corrected functional B97D3, and the ab initio method MP2.[57−63] The results are listed in Table S6. The calculated rmsd of energies from our default method considered all states and were 0.5, 1.4, 1.9, 1.8, and 2.8 kcal/mol for the methods BP/Aug-cc-pVTZ, PBE/6-311++G(d,p), B3LYP/6-311++G(d,p), B97D3/6-311++G(d,p), and MP2/6-311++G(d,p), respectively. These deviations are small and within the range of DFT accuracy that is to be expected in benign cases. Only in the case of MP2 are the deviations somewhat larger, as expected. From these results, we concluded that enhancing the size of the basis set that we used would not have improved the model significantly compared with other inevitable inaccuracies. In addition, variations of the functionals and inclusion of dispersion corrections did not affect the energies of states much. Most importantly, energy barriers hardly changed, and the same catalytic effect was observed with all methods. The value of the largest energy barrier varied less than 2.1 kcal/mol for the mononuclear reaction and less than 1.5 kcal/mol for the binuclear case. The only notable deviation that we observed was that in the binuclear case, the TS for stepwise and concerted reaction pathways were of comparable energy according to PBE calculations, somewhat favoring the concerted pathway. Overall, energy deviations due to functional variations were also consistent with the deviations from mononuclear hydroformylation energies that have been reported previously, as discussed before.

Although finding the reaction pathway and catalytic effect for binuclear hydroformylation was very encouraging, one essential issue required addressing: In our previous work, ref 36, and as described in the introduction (eq 3), the following partial

DOI: 10.1021/cs5019925
ACS Catal. 2015, 5, 2301−2316

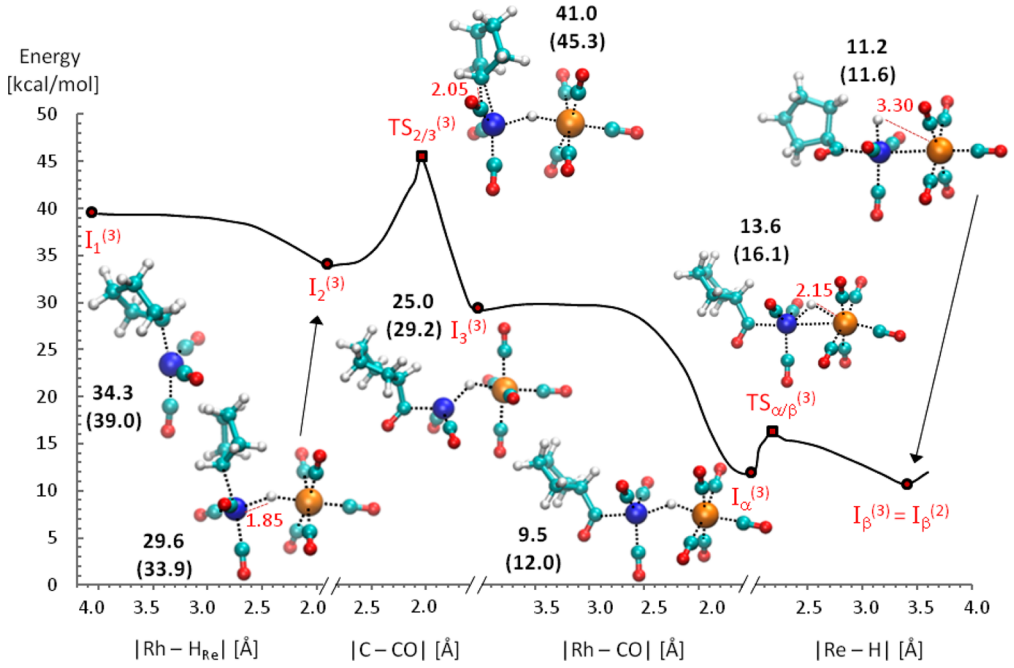

Figure 7. FES from relaxed scan of four steps in reaction: $Rh(CO)_3R + HRe(CO)_5 + CO \leftrightarrow HRhRe(CO)_8RCO$. Energies are given relative to R, that is, $Rh(CO)_4RCO$. The displayed potential was derived directly from FES scanning. The FES in the first reaction step is a function of the distance between rhodium and the hydrogen bonded to rhenium, $|Rh-H_{Re}|$; in the second step, of the distance between the carbon of R (cyclopentyl) that is bonded to rhodium and the carbon of the transferred carbonyl, |C−CO|; in the third step, of the distance between rhodium and the carbon of the approaching carbonyl ligand, |Rh−CO|; and in the fourth step, of the distance between rhenium and the bonded hydrogen, |Re−H|. Structures of ground states and transition states are displayed together with their free energies in black and their potential energies in parentheses. Metalorganic bonds are indicated as dotted lines. Some critical reaction coordinate values for the indentified states are given in red. Structure abbreviations are summarized in Table 1

reaction orders for rhenium-enhanced hydroformylation were measured:

$$r = k_\beta[Rh(CO)_4RCO][HRe(CO)_5][CO]^{-1.6} \quad (7)$$

In eq 7, r is the reaction rate for RCHO production, and k_β is the rate constant. Concentrations were measured as mole fractions. First, eq 7 confirms that the reaction steps considered in this work were, indeed, those that are rate-limiting for the hydroformylation reaction. The most striking feature of eq 7, however, is the noninteger partial reaction order with respect to carbonyl, −1.6. Although the reaction described in this section is consistent with a reaction order of −1 as a result of the release of one carbonyl during the reaction, it alone cannot explain the measured large deviation from −1. In the following section, we therefore need to consider alternative pathways that could explain this anomalous reaction order.

3.4. Binuclear Complex Formation before Migratory Carbonyl Insertion. The measured partial reaction order of −1.6 regarding carbonyl for product formation implies that at least a second reaction pathway that includes the dissociation of two carbonyls must be involved. The assumption seems straightforward that a second activation of the rhodium complex or an activation of rhenium−carbonyl could occur. This assumption was tested, and it was found that tremendous activation energies would be required: For the reaction $Rh(CO)_4RCO \rightarrow Rh(CO)_2RCO + 2CO$, an activation free energy of 34.6 kcal/mol was found. Similarly, for the reaction $Rh(CO)_4RCO \rightarrow Rh(CO)_3R + 2CO$, an activation energy of 34.3 kcal/mol was obtained. For rhenium, an even larger activation energy of 47.7 kcal/mol was found for the reaction $HRe(CO)_5 \rightarrow HRe(CO)_4 + CO$. All these reactions require far more energy than the rate-limiting step in binuclear and even mononuclear hydroformylation and, hence, were excluded as probable reactions.

We analyzed another possibility, instead, in which $HRe(CO)_5$ binds to the rhodium complex before the migratory insertion of carbonyl into the rhodium−cyclopentyl bond. One necessary step in the hydroformylation reaction cycle is the formation of $Rh(CO)_3R$, which is generated after hydrogen insertion into bonded cyclopentene. This species reacts in subsequent steps to the observable ground state **R**, that is, $Rh(CO)_4RCO$, by association of two carbonyl and migratory insertion of one of these carbonyl into the rhodium−cyclopentyl bond: $Rh(CO)_3R + 2CO \leftrightarrow Rh(CO)_4RCO$. The binding of two carbonyls in this reaction connects the ground state, **R**, with alternative reactions that start from $Rh(CO)_3R$ and lead to product formation in such a way that a partial reaction order of −2 with respect to carbonyl can be obtained. In the following, we considered the scenario in which instead of carbonyl, the rhenium complex binds to $Rh(CO)_3R$. We already showed in section 3.2 that a solvophobic effect locally increases the rhenium concentration in the vicinity of rhodium, thereby facilitating a nonchemical binding of these two reactants. The resulting reaction orders will be examined more rigorously in section 3.5.

The FES for the reaction in eq 8 was determined:

$$Rh(CO)_3R + HRe(CO)_5 + CO \leftrightarrow RhRe(CO)_8 + RCHO \quad (8)$$

DOI: 10.1021/cs5019925
ACS Catal. 2015, 5, 2301−2316

Identified intermediates and TS structures together with the corresponding FES are displayed in Figure 7. Energies of the states are listed in Table S7.

The species $Rh(CO)_3R$ is relative to **R** in a high free energy state of +34.3 kcal/mol. Here, we need to keep it in mind that the rhodium-catalyzed hydroformylation reaction exhibits a large overall energy span of ~38 kcal/mol.[78,81] This is mostly due to the large reaction free energy that is released during the reaction cycle that causes an overall steep decrease in the reaction energy profile in the direction of the increasing reaction coordinate.

Rhodium and two carbonyls span the equatorial plane while one coordination site remains empty. Cyclopentyl and another carbonyl are on axial positions. This unsaturated rhodium complex readily binds available ligands. Using the distance between rhodium and hydrogen of the rhenium complex as the reaction coordinate, we found that $HRe(CO)_5$ was bonded barrierless, releasing 4.7 kcal/mol. This intermediate, $\mathbf{I_2}^{(3)}$, corresponds to the previously observed intermediate $\mathbf{I}_\alpha^{(2)}$, but binding a ligand R instead of RCO in an axial position relative to rhodium. Without interactions with the acyl group, as in $\mathbf{I}_\alpha^{(2)}$, the H−Rh−Re angle was found to be with 15.8°, somewhat larger, whereas distances of hydrogen to rhodium and rhenium were similar, 1.85 and 1.83 Å, respectively.

After saturation of the rhodium complex, the FES of migratory insertion of carbonyl into the rhodium−cyclopentyl bond was studied using the distance between the carbon of an equatorial carbonyl and the carbon of cyclopentyl that binds to rhodium as the reaction coordinate, as shown in Figure 7. The activation free energy was 11.4 kcal/mol, and the intermediate $\mathbf{I_3}^{(3)}$ was found at an energy of 25.0 kcal/mol. RCO moved in the unsaturated intermediate $\mathbf{I_3}^{(3)}$ into a ligand position opposite to hydrogen with the acyl group oriented away from the rhenium complex.

Because $\mathbf{I_3}^{(3)}$ is unsaturated, the second carbonyl was bonded almost barrierless to form the intermediate $\mathbf{I}_\alpha^{(3)}$, thereby lowering the energy substantially by 15.5 kcal/mol. The resulting structure corresponds to the previously observed $\mathbf{I}_\alpha^{(2)}$ intermediate, however with the rhodium ligands in different positions. The equatorial plane of rhodium is oriented parallel to the equatorial plane of rhenium. Hydrogen and RCO fill the opposing axial positions in the rhodium complex. This state $\mathbf{I}_\alpha^{(3)}$ is 1.1 kcal/mol higher in energy than the corresponding $\mathbf{I}_\alpha^{(2)}$ state.

Next, as described in the previous section, the rhenium−hydrogen bond was cleaved. The FES was calculated as a function of the distance between rhenium and hydrogen, and a transition to the already observed intermediate $\mathbf{I}_\beta^{(3)} = \mathbf{I}_\beta^{(2)}$ was found. The activation free energy for this step was 4.1 kcal/mol. Continuing the reaction from $\mathbf{I}_\beta^{(2)}$, the next steps are the transitions to $\mathbf{I}_\gamma^{(2)}$ and $\mathbf{P_1}^{(2)}$, which were already discussed in section 3.3.

Overall, the largest single energy barrier for the entire reaction in eq 8 is the carbonyl migratory insertion step (11.4 kcal/mol). In the reaction discussed in section 3.2, the largest single barrier (13.1 kcal/mol) was due to carbonyl release to activate $Rh(CO)_4RCO$ so as to enable binding of the rhenium complex. In both cases, the similar activation energy value was mostly caused by the loss of one carbonyl from the rhodium coordination sphere; that is, it involved a transition from a coordinatively saturated rhodium to an energetically unfavorable unsaturated state.

Although the reaction in the previous section gave rise to a partial reaction order of −1 with respect to carbonyl, the reaction in this section yields a reaction order of −2. This becomes clear when it is considered that the product formation rate of RCHO is proportional to the concentration of $Rh(CO)_3R$, the initial reactant. Unsaturated $Rh(CO)_3R$, however, is too unstable to be observed directly. Nevertheless, it is known that $Rh(CO)_3R$ binds two carbonyls to produce observable $Rh(CO)_4RCO$. That means that $[Rh(CO)_4RCO] \sim [Rh(CO)_3R]\cdot[CO]^2$. Because the rate of [RCHO]-formation (i.e., the product rate) is proportional to $[Rh(CO)_3R]$, it follows that the product rate constant is proportional to $[Rh(CO)_4RCO]\cdot[CO]^{-2}$. It is also important to note that $Rh(CO)_4RCO$ does not react through dissociation of two carbonyl to form $Rh(CO)_3R$ because this would cost a prohibitive amount of energy of 34.3 kcal/mol. The involved kinetics of the overall product formation will be discussed more thoroughly in section 3.5.

For comparison, the FES of migratory insertion of carbonyl according to eq 9 without the presence of a rhenium complex was calculated, as well:

$$Rh(CO)_3R + 2CO \leftrightarrow Rh(CO)_4RCO \quad (9)$$

Structures of intermediates and TS are shown in Figure S10, and the corresponding energies are given in Table S7. The course of the reaction was very similar compared with carbonyl insertion in the binuclear case in eq 8, as expected. After an initial barrierless binding of carbonyl that lowered the energy by 17.1 kcal/mol, carbonyl transfer to cyclopentyl required overcoming an activation free energy of 12.1 kcal/mol, as shown in Figure S10. The height of this barrier is quite similar to the barrier we found for the reaction in eq 8 that involved binding of $HRe(CO)_5$ (11.4 kcal/mol). Thus, the rhenium complex basically did not influence the carbonyl migratory insertion step.

The resulting intermediate at 13.1 kcal/mol, $\mathbf{I_2}^{(4)}$, bonded the second carbonyl barrierless in the next step to reach the ground state, **R**. The unsaturated species, $\mathbf{I_2}^{(4)}$ ($Rh(CO)_3RCO$), is, in fact, a state that is adopted during the first reaction step in eqs 4 and 10, where binding of H_2 and $HRe(CO)_5$ to the rhodium complex were preceded by the dissociation of one carbonyl from **R**, according to the stepwise reaction paths. In other words, at $\mathbf{I_2}^{(4)}$, the hydroformylation reaction branches into three different pathways to produce the product RC(H)O, depending on whether $\mathbf{I_2}^{(4)}$ binds carbonyl, H_2, or $HRe(CO)_5$ in the next step. In addition, as mentioned before in section 3.1, calculated free energies for migratory carbonyl insertion in the mononuclear case were also in good agreement with previously reported computational studies.

In summary, a reaction pathway for the reaction in eq 8 was found in which $HRe(CO)_5$ bonded to the rhodium complex *before* carbonyl migration into the rhodium−cyclopentyl bond and that exhibits a partial reaction order of −2 with respect to carbonyl for product formation. The largest activation barriers for this reaction and the reaction in eq 5, where in the latter case $HRe(CO)_5$ bonded to the rhodium complex *after* carbonyl migration into the rhodium−cyclopentyl bond, were found to be similar in height. That reaction exhibited a partial reaction order of −1 with respect to carbonyl. A combination of these two reactions could explain the overall actually measured reaction order of −1.6, and this is explored in the following section.

DOI: 10.1021/cs5019925
ACS Catal. 2015, 5, 2301−2316

3.5. Analysis of Reaction Kinetics of Hydroformylation Reaction.

In this last section, the overall kinetics of the reactions discussed in sections 3.1−3.4 are derived. In the kinetic model we used, only stable coordinatively saturated rhodium complexes were explicitly considered. Reaction steps that involved unstable unsaturated rhodium complexes were combined with either the preceding or subsequent step into one single step to develop a more concise kinetic model. The resulting reaction steps are summarized in Figure S11, together with corresponding calculated free energy barriers. These explicit reaction steps together with the steady state approximation were used to derive the hydroformylation product formation rate as a function of the observable concentrations of $Rh(CO)_4RCO$, CO, H_2, and $HRe(CO)_5$. Reactions with calculated energy barriers larger than the overall rate-limiting barrier of hydroformylation were neglected, and it was furthermore assumed that the rhenium concentration is negligible compared with the carbonyl concentration, as is the case in experiments.

With these assumptions, the product rate was derived as shown in detail in SI eqs S2−S10, with the final result as follows:

$$\begin{aligned} r &= k_{\mathrm{I}}[Rh(CO)_4RCO][H_2][CO]^{-1} \\ &\quad + k_{\mathrm{II}}[Rh(CO)_4RCO][HRe(CO)_5][CO]^{-1} \\ &\quad + k_{\mathrm{III}}[Rh(CO)_4RCO][HRe(CO)_5][CO]^{-2} \\ k_{\mathrm{I}} &= \frac{k_9 k_{11}}{k_{-9}}, \quad k_{\mathrm{II}} = \frac{k_7 k_8}{k_{-7}}, \quad k_{\mathrm{III}} = 2k_{\mathrm{II}} \end{aligned} \tag{10}$$

Definitions of the rate constants k_i are given in Figure S11b. The first rate constant, k_{I}, describes mononuclear hydroformylation with H_2 (eq 4), and k_{II} and k_{III} describe the binuclear elimination reactions with $HRe(CO)_5$. The second rate constant, k_{II}, describes the reaction of $Rh(CO)_4RCO$ with $HRe(CO)_5$, according to eq 5, which exhibits a reaction order of −1 regarding carbonyl. The third rate constant, k_{III}, describes essentially two reactions with reaction orders of −2 regarding carbonyl: (1) the reaction of $Rh(CO)_3R$ with $HRe(CO)_5$ before the migratory insertion of carbonyl into cyclopentyl (eq 8) and 2, the reaction of $Rh(CO)_3RCO$ with $HRe(CO)_5$ after migratory insertion without *prior* formation of $Rh(CO)_4RCO$.

The product formation rate, r, predicted by our kinetic model in eq 10 is in excellent agreement with our previously measured rate shown in eq 3. The measured reaction order of −1.6 regarding carbonyl implies that k_{II} and k_{III} should be of similar magnitude, and indeed, our model predicts $k_{\mathrm{III}} = 2k_{\mathrm{II}}$.

Overall, the kinetic reaction model could correctly reproduce all measured reaction orders, including, most importantly, the unusual negative noninteger partial reaction order regarding carbonyl. All simplifications used in the model were based on our calculated activation free energies and the additional assumption that the rhenium concentration is very small compared with carbonyl. The reproduction of these unusual reaction orders confirms the identified CBER hydroformylation reaction paths.

4. CONCLUSION

The rate-determining steps of bimetallic hydroformylation of cyclopentene with rhodium and rhenium complexes, solvated in hexane, was studied with DFT and MD simulations. Reaction pathways on FESs derived with DFT were identified and characterized by structures of intermediates and transition states on these paths and their corresponding free energies.

The adequacy of the applied method was successfully verified by a comparison of intermediate and transition state structures and the corresponding energies of mononuclear hydroformylation with previously reported computational results as well as the measured activation free energy. The rate-determining part of mononuclear hydroformylation was characterized by three steps: (1) in $Rh(CO)_4RCO$ substitution of one carbonyl with H_2; (2) cleavage of the H_2 homolytic bond to coordinate both hydrogen atoms individually to rhodium; and (3) transfer of one hydrogen to the acyl group bonded to the reaction substrate, that is, cyclopentyl. The first step was found to be rate-limiting for hydroformylation, with all subsequent steps exhibiting lower energy barriers.

Bimetallic hydroformylation was found to proceed via three very similar steps: (1) activation of the rhodium complex by release of one carbonyl to allow binding of $HRe(CO)_5$ so that hydrogen is shared between the two metal atoms, (2) cleavage of the H−Re bond to complete hydrogen transfer to rhodium and to form a bimetallic bond between rhodium and rhenium, and (3) transfer of the hydrogen to the acyl group bonded to the reaction substrate. A strong stabilization of all intermediates and transition states of rhodium−rhenium complexes compared with substantially less stable rhodium−dihydrogen complexes was observed. This stabilization could be rationalized by the large number of rhenium electrons that allowed coordinative saturation of rhodium upon binding, in contrast to the mere two electrons that are involved in binding of barely polarizable H_2. This stabilization reduced the overall free energy span of the reaction by lowering all energy states with the bonded rhenium complex relative to the ground state of the reaction, thereby causing the overall catalytic effect induced by rhenium. The bimetallic product of the reaction, $RhRe(CO)_9$, was found to be very stable and has indeed been previously identified in bimetallic hydroformylation reactions.

Binding of $HRe(CO)_5$ to the rhodium complex was considered after and before acylation of the hydroformylation substrate. In the first case, the largest activation energy was connected to carbonyl dissociation from $Rh(CO)_4RCO$, whereas for the latter reaction pathway, the largest activation energy was related to the internal carbonyl migration from rhodium to the rhodium−cyclopentyl bond. These two activation energies were of similar height; that is, two separate reaction pathways were found that both contribute to bimetallic hydroformylation. Formation of the bimetallic complex after substrate acylation led to a reaction pathway that exhibited a partial reaction order of −1 with respect to carbonyl, whereas complex formation before substrate acylation involved a partial reaction order of −2 with respect to carbonyl. A combination of these two pathways explained the actually measured unusual reaction order of −1.6. A subsequent analysis of the hydroformylation reaction kinetics was based on identified reaction pathways for mononuclear and binuclear reactions and based on obtained FESs. An expression for the product formation rate was yielded that fully reproduced all previously measured reaction orders of involved observable species.

MD simulations indicated that rhodium and rhenium complexes had a tendency to associate prior to chemical binding. This association was not caused by attractive interactions between rhodium and rhenium complex. Instead, a solvophobic effect strived to minimize the contact between

DOI: 10.1021/cs5019925
ACS Catal. 2015, 5, 2301−2316

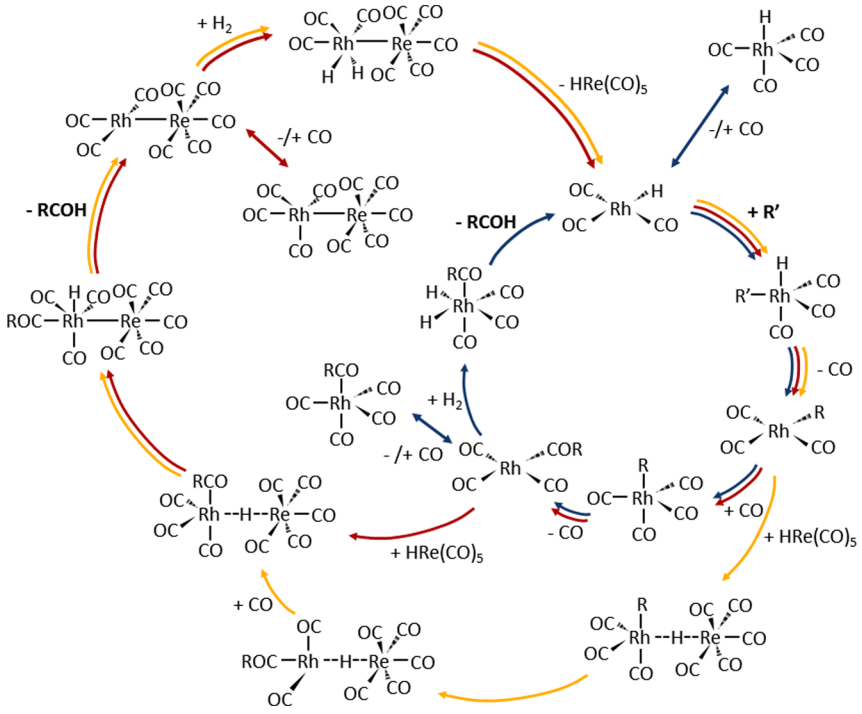

Figure 8. Three identified catalytic cycles of rhodium catalyzed hydroformylation: (1) mononuclear hydroformylation (blue) and (2) binuclear hydroformylation with rhodium−rhenium complex formation after migratory insertion of carbonyl into cyclopentyl (red) and (3) before migratory insertion (orange). Abbreviations: R′ = cyclopentene and R = cyclopentyl.

metal solutes and solvent, which was accomplished by forming the observed weak association. This, in turn, caused a locally elevated concentration of rhenium around rhodium complexes. A consequently increased binding probability of the two metal complexes facilitated hydroformylation further as a secondary effect in addition to the primary catalytic effect caused by a lowering of the overall activation barrier.

The found reaction paths can be described as three interlocking reaction cycles that together constitute the mononuclear and binuclear hydroformylation reaction system, as shown in Figure 8. The first cycle (blue) describes the mononuclear unicyclic reaction involving H_2. The second cycle (red) and third cycle (orange) represent together the CBER, with binding of rhodium−rhenium occurring after and before substrate acylation, respectively.

Overall, to the best of our knowledge, this study presents for the first time a computational analysis of the reaction kinetics of binuclear hydroformylation. The previously unknown underlying molecular reaction mechanism of this CBER system was revealed, and the catalytic effect compared with mononuclear hydroformylation was identified. All key features of previously measured CBER kinetics were reproduced successfully, thereby confirming the findings of this study

■ ASSOCIATED CONTENT

Supporting Information

The following file is available free of charge on the ACS Publications website at DOI: 10.1021/cs5019925.

Force field parametrization for MD simulations (Figures S1−5, Tables S1−3, eq S1); specification of QM/MM simulations; connection between association free energy and initial metal complex concentrations (eqs S2−6); analysis of reaction kinetics of hydroformylation reaction (Figure S11, eqs S7−15); sample sizes along reaction coordinate used for calculation of association free energy (Figure S6); FES for dissociation of axial carbonyl from $Rh(CO)_4RCO$ (Figure S7); dihedral potential for rotation of cyclopentane carboxaldehyde (Figure S8); comparison of FES for mononuclear and binuclear hydroformylation (Figure S9); FES for internal carbonyl migration in $Rh(CO)_4R$ (Figure S10); potential energies and free energies of identified states in all considered reactions (Tables S4−5 and S7); error estimation of DFT method (Table S6); coordinates of all identified intermediates and transition states (PDF)

■ AUTHOR INFORMATION

Corresponding Authors

*E-mail: klahnm@ices.a-star.edu.sg.

*E-mail: marc_garland@ices.a-star.edu.sg.

Notes

The authors declare no competing financial interest.

■ ACKNOWLEDGMENTS

We gratefully acknowledge the provision of computational facilities by the Computational Resource Centre (ACRC), which is part of the Agency for Science, Technology and Research in Singapore (A*STAR).

■ REFERENCES

(1) Masters, C. *Homogeneous Transition-Metal Catalysis: A Gentle Art*; Springer Verlag: Heidelberg, 2013.

(2) Parshall, G. W.; Ittel, S. D. *Homogeneous Catalysis: The Applications and Chemistry of Catalysis by Soluble Transition Metal Complexes*; Wiley Interscience: New York, 1992.

(3) van Leeuwen, P. W. N. M. *Homogeneous Catalysis: Understanding the Art*; Springer Verlag: Heidelberg, 2004.

DOI: 10.1021/cs5019925
ACS Catal. 2015, 5, 2301−2316

(4) Chadwick, J. C.; Rob Duchateau, R.; Freixa, Z.; van Leeuwen, P. W. N. M. *Homogeneous Catalysts: Activity−Stability−Deactivation*; Wiley-VCH: Weinheim, 2011.
(5) Cornils, B.; Herrmann, W. S. *Applied Homogeneous Catalysis with Organometallic Compounds: A Comprehensive Handbook in Two Volumes*; Wiley-VCH: Weinheim, 1996.
(6) King, E. L.; Altman, C. *J. Phys. Chem.* **1956**, *60*, 1375−1378.
(7) Chou, K. C. *J. Biol. Chem.* **1989**, *264*, 12074−12079.
(8) Chou, K. C. *Eur. J. Biochem.* **1980**, *113*, 195−198.
(9) Lam, C. F.; Priest, D. G. *Biophys. J.* **1972**, *12*, 248−256.
(10) Haynes, A.; Mann, B. E.; Gulliver, D. J.; Morris, G. E.; Maitlis, P. M. *J. Am. Chem. Soc.* **1991**, *113*, 8567−8569.
(11) Kamer, P. C. J.; van Rooy, A.; Schoemaker, G. C.; van Leeuwen, P. W. N. M. *Coord. Chem. Rev.* **2004**, *248*, 2409−2424.
(12) Clegg, W.; Eastham, G. R.; Elsegood, M. R. J.; Heaton, B. T.; Iggo, J. A.; Tooze, R. P.; Whyman, R.; Zacchini, S. *Organometalics* **2002**, *21*, 1832−1840.
(13) Heaton, B. T.; Jacob, C.; Monks, G. L.; Hursthouse, M. B.; Ghatak, I.; Somerville, R. G.; Heggie, W.; Page, P. R.; Villax, I. *J. Chem. Soc. Dalton Trans.* **1996**, 61−67.
(14) Jianke Liu, J.; Heaton, B. T.; Iggo, J. A.; Whyman, R. *Angew. Chem., Int. Ed.* **2003**, *43*, 90−94.
(15) Kubis, C.; Ludwig, R.; Sawall, M.; Neymeyr, K.; Börner, A.; Wiese, K.-D.; Hess, D.; Franke, R.; Selent, D. *ChemCatChem* **2010**, *2*, 287−295.
(16) Duckett, S. B.; Newell, C. L.; Eisenberg, R. *J. Am. Chem. Soc.* **1994**, *116*, 10548−10556.
(17) Godard, C.; Duckett, S. B.; Polas, S.; Tooze, R.; Whitwood, A. C. *J. Am. Chem. Soc.* **2005**, *127*, 4994−4995.
(18) Garland, M.; Li, C.; Guo, L. *ACS Catal.* **2012**, *2*, 2327−2334.
(19) Garland, M.; Pino, P. *Organomet.* **1991**, *10*, 1693−1704.
(20) Feng, J.; Garland, M. *Organomet.* **1999**, *18*, 417−427.
(21) Important note: this situation should not be confused with the nonlinear product distribution effects noted by Kagan (refs 22−25) and by others for stereodifferentiating systems, in which instantaneous product selectivity is a function of the local instantaneous concentrations of stereoisomers present in solution.
(22) Puchot, C.; Samuel, O.; Dunach, E.; Zhao, S.; Agami, C.; Kagan, H. B. *J. Am. Chem. Soc.* **1986**, *108*, 2353−2357.
(23) Guillaneux, D.; Zhao, S. H.; Samuel, O.; Rainford, D.; Kagan, H. B. *J. Am. Chem. Soc.* **1994**, *116*, 9430−9439.
(24) Girard, C.; Kagan, H. B. *Angew. Chem., Int. Ed.* **1998**, *37*, 2922−2959.
(25) Satyanarayana, T.; Abraham, S.; Kagan, H. B. *Angew. Chem., Int. Ed.* **2009**, *48*, 456−494.
(26) Hansen, K. B.; Leighton, J. L.; Jacobsen, E. N. *J. Am. Chem. Soc.* **1996**, *118*, 10924−10925.
(27) Schaus, S. E.; Jacobsen, E. N. *Org. Lett.* **2000**, *2*, 1001−1004.
(28) Heck, R.; Breslow, D. *Chem. Ind.* **1960**, *17*, 467.
(29) Heck, R. F.; Breslow, D. S. *J. Am. Chem. Soc.* **1961**, *83*, 4023−4027.
(30) Mirbach, M. F. *J. Organomet. Chem.* **1984**, *265*, 205−213.
(31) Konsler, R. G.; Karl, J.; Jacobsen, E. N. *J. Am. Chem. Soc.* **1998**, *120*, 10780−10781.
(32) Liu, G. W.; Li, C. Z.; Guo, L. F.; Garland, M. *J. Catal.* **2006**, *237*, 67−78.
(33) Haynes, A.; Maitlis, P. M.; Morris, G. E.; Sunley, G. J.; Adams, H.; Badger, P. W.; Bowers, C. M.; Cook, D. B.; Elliott, P. I. P.; Ghaffar, T.; Green, H.; Griffin, T. R.; Payne, M.; Pearson, J. M.; Taylor, J. M.; Vickers, P. W.; Watt, R. J. *J. Am. Chem. Soc.* **2004**, *126*, 2847−2861.
(34) Li, C.; Widjaja, E.; Garland, M. *J. Am. Chem. Soc.* **2003**, *125*, 5540−5548.
(35) Li, C.; Widjaja, E.; Garland, M. *Organomet.* **2004**, *23*, 4131−4138.
(36) Li, C.; Chen, L.; Garland, M. *J. Am. Chem. Soc.* **2007**, *129*, 13327−13334.
(37) Li, C.; Chen, L.; Garland, M. *Adv. Synth. Catal.* **2008**, *350*, 679−690.
(38) Li, C.; Cheng, S.; Tjahjono, M.; Schreyer, M.; Garland, M. *J. Am. Chem. Soc.* **2010**, 4589−4599.
(39) Li, C.; Chen, L.; Widjaja, E.; Garland, M. *Catal. Today* **2010**, *155*, 261−265.
(40) Li, C.; Gao, F.; Cheng, S.; Tjahjono, M.; van Meurs, M.; Tay, B. Y.; Jacob, C.; Guo, L. F.; Garland, M. *Organomet.* **2011**, *30*, 4292−4296.
(41) Abramo, G. P.; Marks, T. J. *J. Am. Chem. Soc.* **2002**, *124*, 13966−13967.
(42) Yuen, H. F.; Marks, T. J. *Organomet.* **2009**, *28*, 2423−2440.
(43) Heaton, B. *Mechanisms in Homogeneous Catalysis: A Spectroscopic Approach*; Wiley: Weinheim, Germany, 2005.
(44) Cornils, B.; Herrmann, W. A.; Wong, C. H.; Zanthoff, H. W. *Catalysis from A to Z: A Concise Encyclopedia*; Wiley-VCH: Weinheim, 2013; pp 434−435.
(45) Li, C.; Guo, L.; Garland, M. *Organometalics* **2004**, *23*, 5275−5279.
(46) Frisch, M. J.; Trucks, G. W.; Schlegel, H. B.; Scuseria, G. E.; Robb, M. A.; Cheeseman, J. R.; Scalmani, G.; Barone, V.; Mennucci, B.; Petersson, G. A.; Nakatsuji, H.; Caricato, M.; Li, X.; Hratchian, H. P.; Izmaylov, A. F.; Bloino, J.; Zheng, G.; Sonnenberg, J. L.; Hada, M.; Ehara, M.; Toyota, K.; Fukuda, R.; Hasegawa, J.; Ishida, M.; Nakajima, T.; Honda, Y.; Kitao, O.; Nakai, H.; Vreven, T.; Montgomery, J. A.; Peralta, J. E.; Ogliaro, F.; Bearpark, M.; Heyd, J. J.; Brothers, E.; Kudin, K. N.; Staroverov, V. N.; Kobayashi, R.; Normand, J.; Raghavachari, K.; Rendell, A.; Burant, J. C.; Iyengar, S. S.; Tomasi, J.; Cossi, M.; Rega, N.; Millam, J. M.; Klene, M.; Knox, J. E.; Cross, J. B.; Bakken, V.; Adamo, C.; Jaramillo, J.; Gomperts, R.; Stratmann, R. E.; Yazyev, O.; Austin, A. J.; Cammi, R.; Pomelli, C.; Ochterski, J. W.; Martin, R. L.; Morokuma, K.; Zakrzewski, V. G.; Voth, G. A.; Salvador, P.; Dannenberg, J. J.; Dapprich, S.; Daniels, A. D.; Farkas, O.; Foresman, J. B.; Ortiz, J. V.; Cioslowski, J.; Fox, D. J. *Gaussian 09, Rev. A.1*; Gaussian Inc.: Wallingford CT, 2009.
(47) Becke, A. D. *Phys. Rev. A* **1988**, *38*, 3098−3100.
(48) Perdew, J. P. *Phys. Rev. B* **1986**, *33*, 8822−8824.
(49) Krishnan, R.; Binkley, J. S.; Seeger, R.; Pople, J. A. *J. Chem. Phys.* **1980**, *72*, 650−654.
(50) Andrae, D.; Häußermann, U.; Dolg, M.; Stoll, H.; Preuß, H. *Theor. Chem. Acc.* **1990**, *77*, 123−141.
(51) Hay, P. J.; Wadt, W. R. *J. Chem. Phys.* **1985**, *82*, 270−283.
(52) Scalmani, G.; Frisch, M. J. *J. Chem. Phys.* **2010**, *132*, 114110.
(53) Boys, S. F.; Bernardi, F. *Mol. Phys.* **1970**, *19*, 553−566.
(54) Lendvay, G.; Mayer, I. *Chem. Phys. Lett.* **1998**, *297*, 365−373.
(55) Alvarez-Idaboy, J. R.; Galano, A. *Theor. Chem. Acc.* **2010**, *126*, 75−85.
(56) Papajak, E.; Truhlar, D. G. *J. Chem. Theory Comput.* **2011**, *7*, 10−18.
(57) Dunning, T. H. *J. Chem. Phys.* **1989**, *90*, 1007−1023.
(58) Kendall, R. A.; Dunning, T. H.; Harrison, R. J. *J. Chem. Phys.* **1992**, *96*, 6796−6806.
(59) Perdew, J. P.; Burke, K.; Ernzerhof, M. *Phys. Rev. Lett.* **1996**, *77*, 3865−3868.
(60) Becke, A. D. *J. Chem. Phys.* **1993**, *98*, 5648−5652.
(61) Grimme, S. *J. Comput. Chem.* **2006**, *27*, 1787−1799.
(62) Grimme, S.; Ehrlich, S.; Goerigk, L. *J. Comput. Chem.* **2011**, *32*, 1456−1465.
(63) Head-Gordon, M.; Pople, J. A.; Frisch, M. J. *Chem. Phys. Lett.* **1988**, *153*, 503−506.
(64) Klähn, M.; Rosta, E.; Warshel, A. *J. Am. Chem. Soc.* **2006**, *128*, 15310−15323.
(65) Berendsen, H. J. C.; van der Spoel, D.; van Drunen, R. *Comput. Phys. Commun.* **1995**, *91*, 43−56.
(66) Lindahl, E.; Hess, B.; van der Spoel, D. *J. Mol. Model.* **2001**, *7*, 306−317.
(67) van der Spoel, D.; Lindahl, E.; Hess, B.; Groenhof, G.; Mark, A. E.; Berendsen, H. J. C. *J. Comput. Chem.* **2005**, *26*, 1701−1718.
(68) Hess, B.; Kutzner, C.; van der Spoel, D.; Lindahl, E. *J. Chem. Theory Comput.* **2008**, *4*, 435−447.

DOI: 10.1021/cs5019925
ACS Catal. 2015, 5, 2301−2316

(69) Jorgensen, W. L.; Maxwell, D. S.; Tirado-Rives, J. *J. Am. Chem. Soc.* **1996**, *118*, 11225−11236.
(70) Kaminski, G. A.; Friesner, R. A.; Tirado-Rives, J.; Jorgensen, W. L. *J. Phys. Chem. B* **2001**, *105*, 6474−6487.
(71) Hess, B.; Bekker, H.; Berendsen, H. J. C.; Fraaije, J. G. E. M. *J. Comput. Chem.* **1997**, *18*, 1463−1472.
(72) Bussi, G.; Donadio, D.; Parrinello, M. *J. Chem. Phys.* **2007**, *126*, 014101.
(73) Berendsen, H. J. C.; Postma, J. P. M.; van Gunsteren, W. F.; DiNola, A.; Haak, J. *J. Chem. Phys.* **1984**, *81*, 3684.
(74) Darden, T.; York, D.; Pedersen, L. *J. Chem. Phys.* **1993**, *98*, 10089.
(75) Essman, U.; Perera, L.; Berkowitz, T.; Darden, T.; Lee, H.; Pedersen, L. *J. Chem. Phys.* **1995**, *103*, 8577−8593.
(76) Kumar, S.; Rosenberg, J. M.; Bouzida, D.; Swendsen, R. H.; Kollman, P. A. *J. Comput. Chem.* **1992**, *13*, 1011−1021.
(77) Hub, J. S.; de Groot, B. L.; van der Spoel, D. *J. Chem. Theory Comput.* **2010**, *6*, 3713−3720.
(78) Sparta, M.; Børve, K. J.; Jensen, V. R. *J. Am. Chem. Soc.* **2007**, *129*, 8487−8499.
(79) Amatore, C.; Jutland, A *J. Organomet. Chem.* **1999**, *576*, 254−278.
(80) Kozuch, S.; Shaik, S. *J. Am. Chem. Soc.* **2006**, *128*, 3355−3365.
(81) Gleich, D.; Hutter, J. *Chem.—Eur. J.* **2004**, *10*, 2435.
(82) Hebrard, F.; Kalck, P. *Chem. Rev.* **2009**, *109*, 4272−4282.
(83) Maeda, S.; Morokuma, K. *J. Chem. Theory Comput.* **2012**, *8*, 380−385.

DOI: 10.1021/cs5019925
ACS Catal. 2015, 5, 2301−2316